Bidirectional interconversion between mutually exclusive tumorigenic and drug-tolerant melanoma cell phenotypes

Yuntian Zhang[1], Rachel L Belote[2,†], Marcus A Urquijo[2,3,†], Maike M. K. Hansen[4], Miroslav Hejna[5,6], Tarek E. Moustafa[7], Tong Liu[2,8], Devin Lange[9], Fatemeh Vand-Rajabpour[10], Matthew Chang[11-14], Brian K. Lohman[2], Chris Stubben[2], Xiaoyang Zhang[2,3], Leor S. Weinberger[15,16], Matthew W VanBrocklin[2,17], Douglas Grossman[2,8], Alexander Lex[2,9], Rajan Kulkarni[11-14], Thomas Zangle[2,7] and Robert L. Judson-Torres[2,3,8,] *

Affiliations

[1]Helen Diller Family Comprehensive Cancer Center, University of California, San Francisco, CA 94158, USA

[2]Huntsman Cancer Institute, University of Utah, Salt Lake City, UT 84112, USA

[3]Department of Oncological Sciences, University of Utah School of Medicine, Salt Lake City, UT 84103, USA

[4]Radboud University, Institute for Molecules and Materials, Heyendaalseweg 135, 6525 AJ Nijmegen, the Netherlands

[5]Department of Physics, University of Illinois at Urbana-Champaign, Urbana, IL 61801, USA

[6]Carl R. Woese Institute for Genomic Biology, University of Illinois at Urbana-Champaign, Urbana, IL, 61801, USA

[7]Department of Chemical Engineering, University of Utah, Salt Lake City, UT 84103, USA

[8]Department of Dermatology, University of Utah School of Medicine, Salt Lake City, UT 84132, USA

[9]SCI Institute and Kahlert School of Computing, University of Utah, Salt Lake City, UT 84112, USA

[10]Department of Medical Genetics, School of Medicine, Tehran University of Medical Sciences, Tehran, Iran.

[11]Department of Dermatology, Oregon Health and Science University, Portland, OR 97239, USA.

[12]Departments of Biomedical Engineering and Oncological Sciences, Oregon Health and Science University, Portland, OR 97239, USA.

[13]Cancer Early Detection Advanced Research Center, Knight Cancer Institute, Oregon Health and Science University, Portland, OR 97239, USA.

[14]Operative Care Division, VA Portland Health Care System, Portland, OR 97239, USA.

[15]Gladstone Center for Cell Circuitry, Gladstone Institutes, San Francisco, CA 94158, USA

[16]Departments of Pharmaceutical Chemistry and Biochemistry and Biophysics, University of California, San Francisco, CA 94158, USA

[17]Department of Surgery, University of Utah School of Medicine, Salt Lake City, UT 84132, USA

†Indicates equal contribution.

*Correspondence and Lead Contact: judsontorreslab@gmail.com

Abstract

Human cancers can exhibit phenotype switching, resulting in cells that are more metastatic or that are more tolerant to treatment. However, the relationship between these aggressive states is not well understood. We investigated the dynamics of phenotypic switching in human melanoma cells by monitoring the fluorescent activity from a transgenic reporter of BRN2 promoter activation. Melanoma cells exhibit heterogeneous BRN2 expression patterns that are reestablished upon isolation and clonal outgrowth. Specifically, stable BRN2 expression was generally inherited over multiple generations while undergoing occasional bidirectional interconversion. We found that BRN2 low cells were required for tumor initiation and metastasis in animal engraftment assays but were more sensitive to targeted BRAF inhibition. In contrast, the BRN2 high state was not tumorigenic, but entry into this state was uniform and persistent among cells tolerant to targeted BRAF therapy. Single-cell RNA sequencing analyses revealed core programs exclusive to either the BRN2 high or low cells, each of which is present in *ex vivo* tumors, demonstrating the physiological relevance of these states. Our findings emphasize that one challenge of effectively targeting phenotype switching in melanoma as a therapeutic strategy could be balancing distinct aggressive phenotypes so that sensitizing tumors to BRAF inhibition does not inadvertently lead to further dissemination.

Teaser

Unraveling melanoma's shape-shifting behavior: insights into how cancer cells swap between metastasis and drug evasion.

Introduction

Phenotype switching refers to a consequential alteration in the transcriptional programs and behaviors of a cell in the absence of additional genetic changes. This process gives rise to tumor heterogeneity and contributes to tumor initiation, primary growth, progression, and metastasis[1,2]. In particular, a variety of phenotypes have been characterized during the progression of cutaneous melanoma - a disproportionally lethal skin cancer arising from neural crest-derived pigmented cells called melanocytes[1,3–15]. Four transcriptional programs frequently associated with melanoma phenotype switching are those controlled by the transcription factors MITF, SOX10 and BRN2 (aliases include POU3F2 and N-OCT3) and the receptor tyrosine kinase AXL[8,16–34]. MITF is considered a master-regulator of the melanocytic lineage and regulates melanocyte differentiation and pigmentation[35]. SOX10 is a well-established activator of MITF expression, but is also critical for the neural crest stem cell (NCSC) program that precedes melanocyte specification during development and plays complex roles in melanoma proliferation and progression[34,36–38]. While the relative expression of the MITF and AXL programs are often described as mutually exclusive[16–19], their relationship with the BRN2 program is less consistent. BRN2 is a lineage-essential transcription factor that is expressed in melanocyte precursors, silenced in differentiated melanocytes, and heterogeneously reactivated in the dermal component of both benign and malignant melanocytic tumors[20–23]. In both development and disease, BRN2 expression is often, but not always, associated with migration and invasion[24–28]. One model suggests that BRN2 and MITF represent the two poles of a molecular switch that toggles between the distinct states of invasive and proliferative phenotypes[21,27,29]. However, melanoma cells are capable of simultaneous invasion and division[39]. Conditions that induce the invasive phenotype or oppose the proliferative MITF program do not necessitate increased BRN2 expression, nor are BRN2 and AXL obligatorily co-expressed[17,24,26]. In addition, dependent on the context, the genes can also present reciprocal activation or no relationship at all[24,26–32]. These observations collectively challenge the model of a compulsory mutually exclusive MITF/BRN2 axis. Regardless of its relationship to MITF, BRN2 expression oscillates between distinct stages of metastasis *in vivo*, and the gene itself can serve to either promote or suppress melanoma

progression[8,23,33]. Thus, dynamic BRN2 expression appears important for melanoma progression, but the contexts in which it serves to promote or restrain aggressive disease remain obscure.

Therapeutic strategies for pharmacological targeting and suppressing specific cellular phenotypes are being explored for combatting melanoma progression[1,14,34,40–44]. However, given that the relationships between distinct and significant phenotypes remain incompletely characterized such strategies could yield unintended, and potentially harmful, consequences. For example, multiple therapeutic resistance phenotypes and multiple tumorigenic stem-like phenotypes have been described[8,16–33,43–45]. Cell surface antigens used to purify tumorigenic cells in some studies prove unreliable in others, and the relationship between drug-tolerant and tumorigenic phenotypes remains incompletely understood[46–54]. We sought to characterize the dynamics of switching between tumorigenic and targeted therapy-tolerant melanoma phenotypes. We reveal a relationship of mutual exclusivity, such that the enrichment of one phenotype necessitates the depletion of the other. Each phenotype was generally inherited within a lineage but could also undergo bidirectional interconversion to re-establish a phenotypic equilibrium within the population. This work reveals potentially significant complications for therapeutic strategies aimed at diverting cells from a drug-tolerant phenotype, as the practice could inadvertently induce a pro-metastatic phenotype.

Results

Phenotypic equilibrium is established within clonal human melanoma lines

To monitor the dynamics of phenotypic switching we generated a fluorescent reporter construct for the promoter activity of *BRN2*. We performed ATAC-seq in the human melanoma cell line, 624-Mel, to identify the region of open chromatin upstream of the gene. We defined the proximal active promoter region as spanning from ~ 817 base pairs (bp) upstream of the transcriptional start site (TSS) to ~ 195 bp into the untranslated transcript, consistent with prior reports in mouse (**Fig. 1A**)[8]. We cloned this region into a selectable lentiviral mammalian expression construct, adjacent to a nuclear localization signal (NLS) tagged mCherry (**Fig. 1A**) and transduced three human melanoma cell lines – 624-Mel, WM793, and SK-MEL-28. After antibiotic selection, we isolated clonal populations. For each line, clonal growth initially expanded into populations of uniform mCherry expression. Over two weeks in culture, each uniform population yielded bimodal distributions of mCherry expression, such that mCherry low populations begot mCherry high populations and vice versa (**Fig. 1B & Supplemental Fig. S1**). To confirm the fidelity of the reporter we FACS-isolated mCherry low and high cells from each population. The mCherry low cells expressed 2-3-fold less BRN2 protein and mRNA as compared to matched mCherry high cells (**Fig. 1C-D**). Single-molecule (sm)FISH confirmed a significant correlation between the expression of the mCherry transcript and endogenous BRN2 transcript (**Fig. 1E**). Using smFISH, we compared the distributions of BRN2 transcript counts from clonal 624-Mel reporter lines to the parental line (**Fig. 1F**). We detected 3-9 copies of BRN2 mRNA per mCherry low cell, whereas the mCherry high cells presented a broader distribution of 12-60 copies per cell. The distribution of BRN2 transcript within the parental line encompassed the merged distributions of the clones, confirming the clonal populations were representative of the parental BRN2 expression distribution. We performed immunofluorescence for BRN2 in the parental populations and observed similar bimodal expressions (**Fig. 1G**). We generated clonal

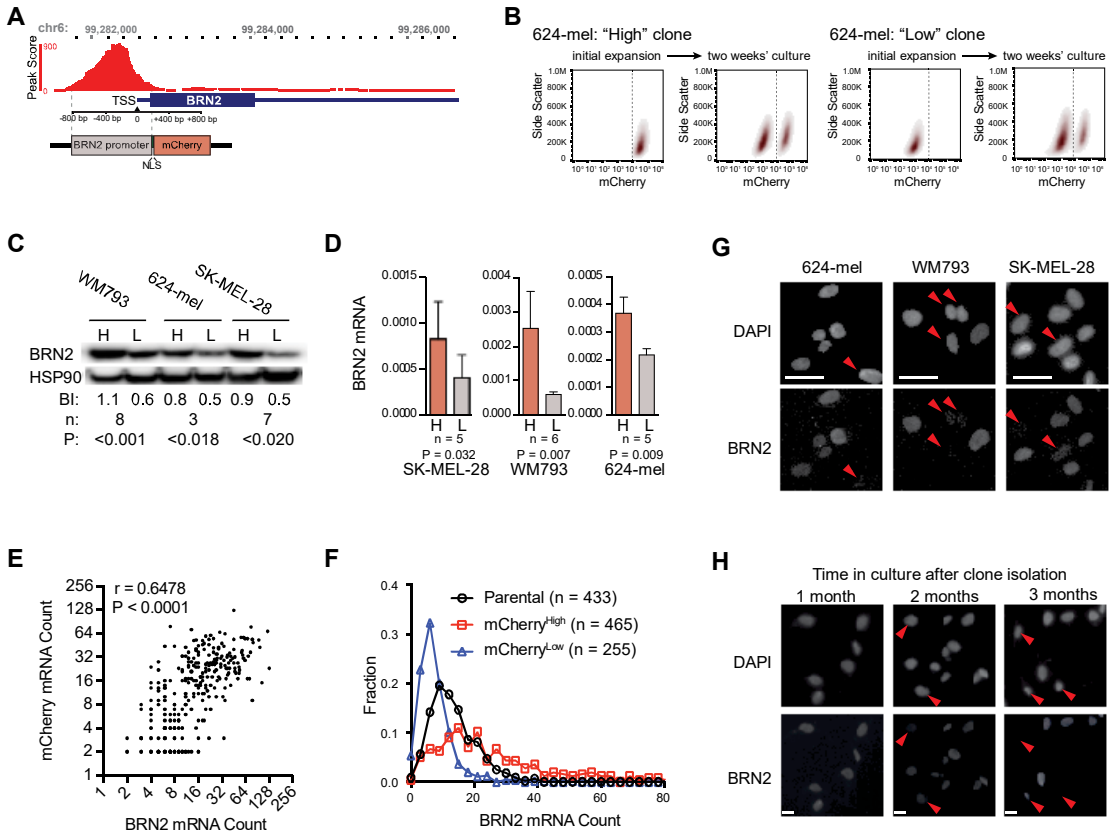

Figure 1: Gradual establishment of BRN2 expression equilibrium in human melanoma cells. A) ATACseq peak scores from the BRN2 locus (top) and schematic of reporter construct (bottom). TSS, transcriptional start site. NLS, nuclear localization signal. B) Flow analysis of clonally expanded then serially cultured 624-mel cells with the BRN2 reporter. See Supplemental Figure S1 for more examples. C) Western blot of BRN2 and HSP90 loading control in reporter high (H) and reporter low (L) cells from indicated cell lines. BI, average blot intensity. n, number of independent lysates. P, two-tailed t test P value. D) Average and SD of ΔCt between probes for BRN2 and RPL37A transcript RT-qPCR probe sets. n, number of independent RNA preparations, P, two-tailed t test P value. E) Single molecule fluorescent in situ hybridization (smFISH) BRN2 and mCherry transcript counts from individual 624-mel cells. r, Pearson's correlation coefficient. P, two-tailed P value. F) Distribution of BRN2 smFISH transcript counts in 624-mel cells as fraction of total population. n, number of individual cells. G) Images of BRN2 IF staining of indicated cell lines. Red arrowheads indicate cells with poor BRN2 expression. H) Images of BRN2 IF in clonal expansion of 624-mel cells at 1 month, 2 months and 3 months. Scale bars = 20μm.

populations of the parental 624-Mel line via limiting dilution and monitored the BRN2 protein expression over time in culture (**Fig. 1H**). BRN2 expression was uniform in short-term culture and became more heterogenous over time, consistent with the gradual redistribution of mCherry expression we observed in the clones. We conclude that melanoma cells exhibit a heterogenous BRN2 expression pattern that is reestablished upon isolation and clonal outgrowth.

While culturing, we noticed the cells expressing less mCherry (referred to henceforth as Low^{BRN2}) were smaller and more uniform in appearance as compared to the $High^{BRN2}$ cells (**Fig. 2A**). We analyzed isolated Low^{BRN2} and $High^{BRN2}$ cells with digital holographic cytometric feature classification - a method that compares aggregate morphological features of cells[55–57]. In all lines, Low^{BRN2} cells were morphologically distinct from $High^{BRN2}$ cells (P<0.0001) (**Fig. 2B**). We explored phenotypic differences between the lines using live imaging. Low^{BRN2} cells divided more rapidly than $High^{BRN2}$ cells (19.5 hours versus 25.5 hours, respectively, P-value = 0.0028) (**Fig. 2C**). Neither line presented greater random motility (**Fig. 2D**). To gain greater insight into transcriptional changes between the $High^{BRN2}$ and Low^{BRN2} cells, we FACS-purified each

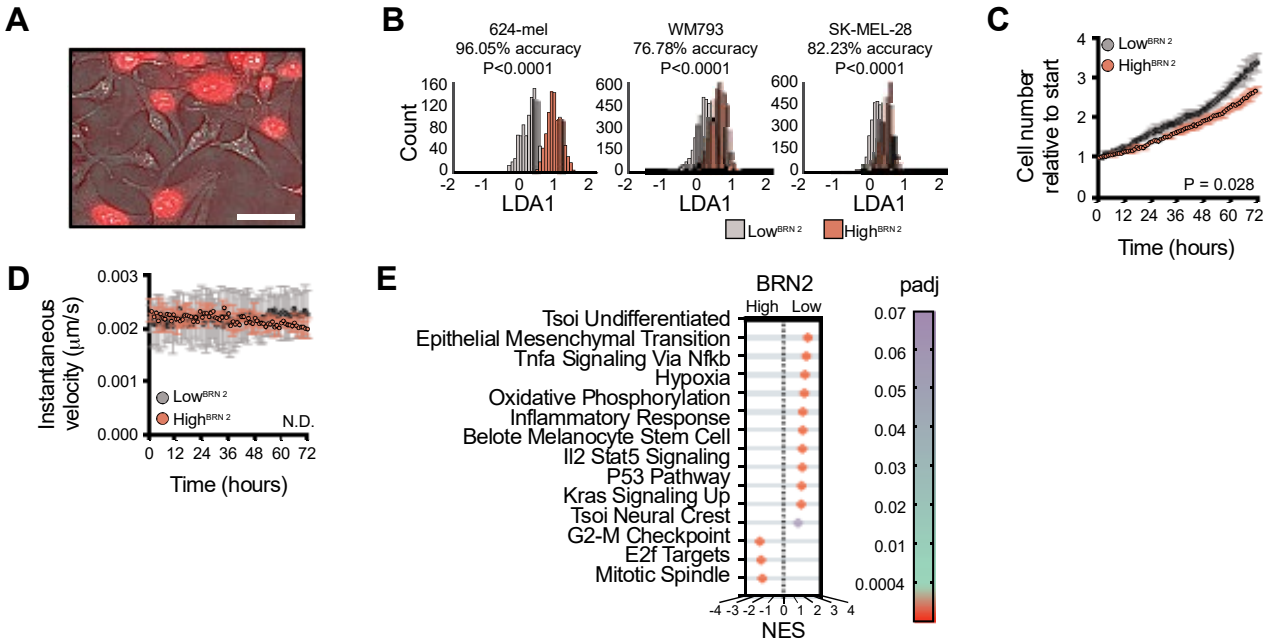

Figure 2: Comparison of phenotype, morphology and gene expression between BRN2 high and low cells. A) Image of clonal 624-mel population expression mCherry reporter. Scale bar = 50μm**.** B) Classification of indicated cells into mCherry high ($High^{BRN2}$) and mCherry low (Low^{BRN2}) populations using a linear discriminant analysis of morphologic features. Population distribution, classification accuracy and p value from two-tailed t test (P) are shown. C) Cell number over time, relative to start of $High^{BRN2}$ and Low^{BRN2} cells. Population mean, standard deviation and p value from two-tailed t test comparing final time point of three independent experiments are shown. D) Instantaneous cell velocity over time from experiments depicted in C). E) Gene set enrichment analysis (GSEA) comparing DE genes between $High^{BRN2}$ and Low^{BRN2} cells to published signatures of melanocyte signaling and differentiation from Belote et al., 2021 and Tsoi et al., 2018 and to Molecular Signature Database Hallmark gene sets. Normalized enrichment score (NES); adjusted p-value (padj).

population and performed bulk RNAseq. 140 genes were differentially expressed (DE) with Log2 fold change ≥ 1.5 or ≤ -1.5 and adjusted P-value < 0.0005 (**Supplemental Table S1**). Gene set enrichment analysis (GSEA) comparing DE genes to the Hallmark pathways[58] and to gene sets previously reported in association with melanoma phenotype switching or melanocyte development[13,59] revealed significant enrichments for signatures of the epithelial to mesenchymal transition, hypoxia, inflammatory response, p53 signaling, undifferentiated melanoma cells, neural crest melanoma cells, and human melanocyte stem cells (MSC) in the Low^{BRN2} population – all pathways previously associated with stem-like tumorigenic cells (**Fig. 2E**). We conclude that clonal human melanoma lines reestablish phenotypic equilibrium in culture between a more stem-like population (Low^{BRN2}) and a less stem-like population ($High^{BRN2}$).

Phenotypes are inherited and equilibrium is established via bidirectional interconversion

Evidence for melanoma phenotype switching in prior studies has included the classification of single cells or populations of cells into subgroups based upon both gene expression and cell behavior as well as the emergence of these subgroups in selective conditions, during tumor progression, or upon molecular or genetic manipulation[8,26,29,33]. However, the live monitoring of a single cell undergoing the conversion from one phenotype to another has not been documented in human melanoma cells to our knowledge. As such, the kinetics of phenotype switching in homeostatic conditions, including how switching is related to cell growth and division, remain largely uncharacterized.

173 We used ptychography[60] – a form of quantitative phase imaging – coupled with fluorescent
174 microscopy to monitor heterogenous 624-mel cultures expressing the mCherry reporter. Cells
175 were monitored for 48 hours at 30-minute intervals. We tracked the lineages of cells identified at
176 timepoint zero and monitored mCherry expression level and cell morphology (**Fig. 3A-C**).

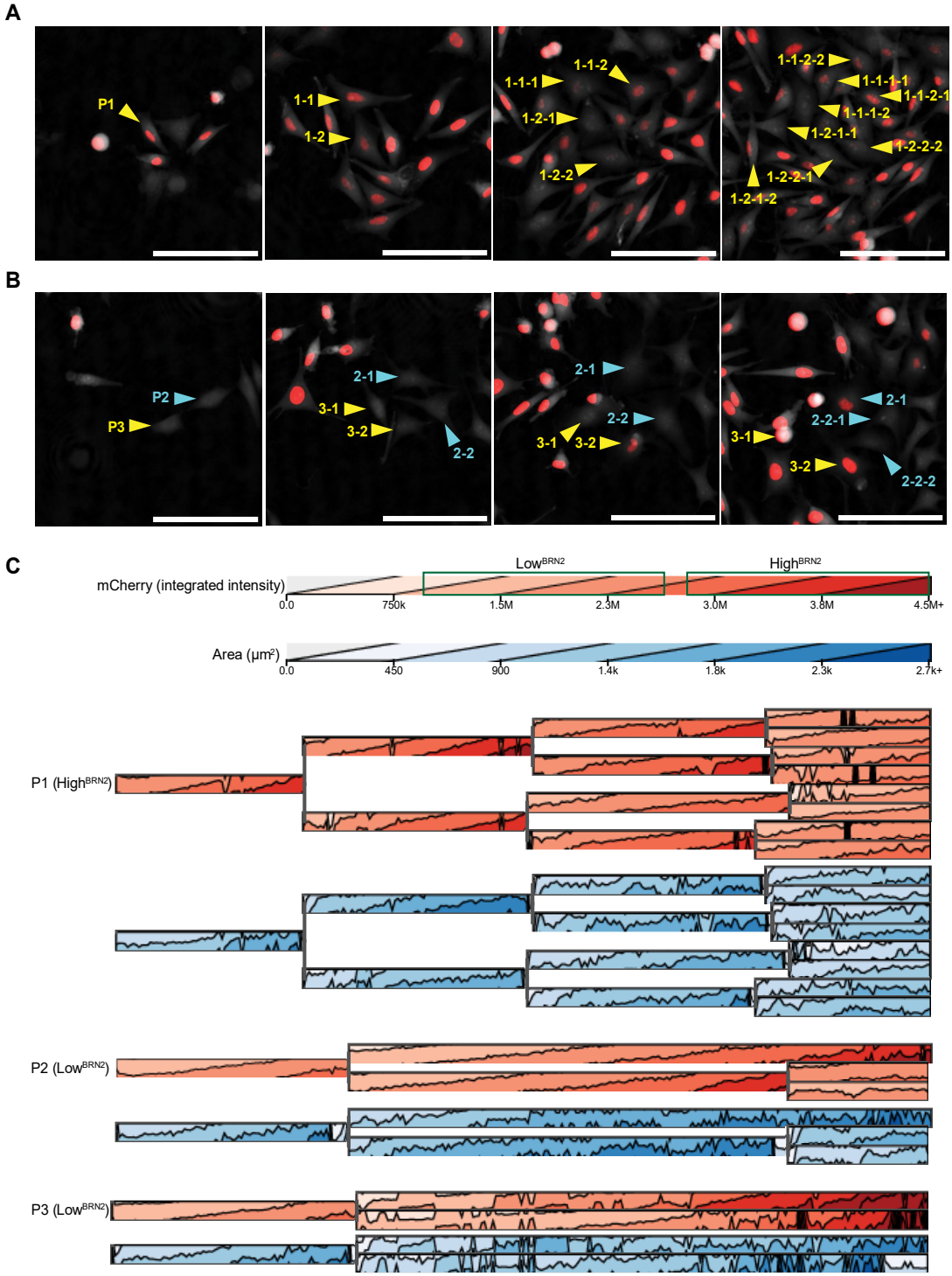

Figure 3: Phenotypes are both inherited and undergo spontaneous bidirectional interconversion. A-B) Stills from representative Supplemental Videos 1 and 2, respectively, taken every 30 minutes for 2 days. Parental cells (P1, P2, P2) are highlighted in each (left column) and tracked through one or more divisions (yellow and blue arrow heads). Scale bar = 200µm. C) Integrated mCherry intensity and cell area over time of lineages highlighted in (A), plotted as lineage tracking horizon charts. Green rectangles indicate range of mCherry expression during cell growth and division for High^{BRN2} and Low^{BRN2} cells. A visual key to horizon chart interpretation is in Supplemental Figure S2.

Overall, mCherry expression was stable in most cells over multiple divisions (**Supplemental Videos V1-V2**). Expected fluctuations of mCherry that corresponded to the accumulation and subsequent halving of cell mass associated with growth and division were observed with each cell cycle, but these changes in mCherry expression were minor in comparison to the difference in mCherry expression between the two states (**Fig. 3C**). During most divisions, the mCherry expression level of the parental cell was inherited by each daughter cell, resulting in clusters of either High^{BRN2} or Low^{BRN2} cells. Interconversions in both directions were also captured. For example, we observed High^{BRN2} parental cells giving rise to both High^{BRN2} and Low^{BRN2} daughter cells (**Fig. 3A**, cells 1-1, 1-1-1, and 1-1-2) and the subsequent reverse transition of Low^{BRN2} progeny back to a High^{BRN2} phenotype (**Fig. 3A**, cells 1-1-1-1 and 1-2-1-2). In many cases, the transitions occurred as apparent asymmetric divisions, although we also observed the gradual increase of mCherry expression in Low^{BRN2} cells outside the context of division (**Fig. 3B**, cell 3-2). The changes in mCherry expression were coupled with the expected changes in cell morphology, with mCherry high cells adopting a larger and flatter morphology (**Fig. 3C**, area), further demonstrating the fidelity of the reporter in marking distinct cell phenotypes. These observations confirm that phenotype switching occurs in human melanoma cells in homeostatic conditions. The two phenotypes can be inherited and typically remain stable through multiple cell divisions, though sporadic bidirectional phenotype switches do occur.

The Low^{BRN2} phenotype is tumorigenic

We next investigated whether phenotypes associated with either Low^{BRN2} or High^{BRN2} cells might impact melanoma growth or metastatic behavior. One phenotype associated with aggressive disease is the ability to initiate tumorigenesis or metastasis upon engraftment into mice[61]. The enrichment for neural crest, MSC, hypoxia and other similar programs in the Low^{BRN2} cells (**Fig. 2E**) is consistent with a stem-like phenotype[30,32]. We, therefore, tested tumorigenicity using a graft efficiency assay. Reporter 624-mel clones were transduced with a constitutively active luciferase construct. Two million FACS-enriched Low^{BRN2} or High^{BRN2} cells were isolated via FACS and implanted subcutaneously into NOD *scid* gamma mice. Tumor growth was monitored over five weeks (**Fig. 4A**). Mice implanted with Low^{BRN2} cells formed tumors in 100% (7/7) of mice compared to 14.3% (1/7, $P = 0.0018$) of mice implanted with High^{BRN2} cells (**Fig. 4B-C**). After five weeks, surviving mice were sacrificed, and the brain, lungs, and liver were imaged (**Fig. 4D**). All mice engrafted with Low^{BRN2} cells presented distal metastatic dissemination based on luciferase expression, as compared to a single mouse in the High^{BRN2} cohort ($P = 0.0101$) (**Fig. 4E**). Thus, Low^{BRN2} cells were more competent for initiating tumor growth and metastasis upon engraftment.

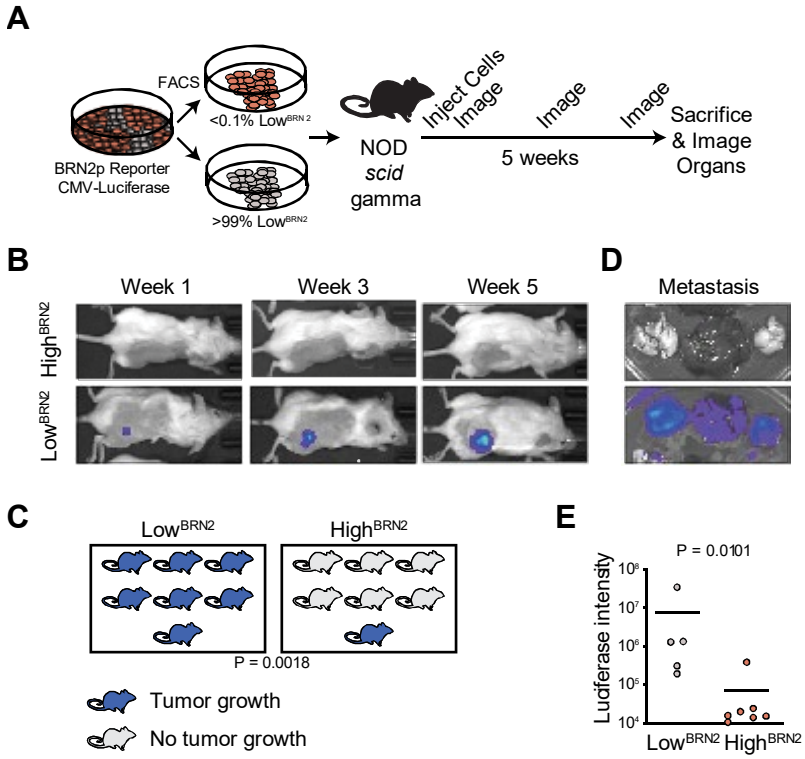

Figure 4: The BRN2 low state is tumorigenic. A) Schematic of graft efficiency assay. Clonal 624-mel cultures were either depleted (red) or enriched (grey) for Low^{BRN2} cells and implanted into NOD scid gamma mice. Luciferase imaging was conducted 1, 3, and 5 weeks after implantation followed by sacrifice and organ imaging. B) Representative images of luminescence at indicated time points. C) Percent of mice with successful grafts after 5 weeks. P, two-tailed Fisher's exact test P value with 0.98 power. D) Representative images of organ luminescence. E) Average (line) and individual summations of luciferase intensity in brain, liver, and lungs. P, two-tailed t test P value.

Tolerance to targeted BRAF^{V600E} inhibition excludes the Low^{BRN2} phenotype

In addition to primary growth and metastasis, another phenotype associated with aggressive disease is resistance to therapeutic intervention. Each of the three lines selected for this study harbors the *BRAF^{V600E}* oncogenic driver, identified in approximately half of all melanomas[62] (confirmed by digital droplet RT-qPCR, data not shown). Small molecules that selectively inhibit the mutated BRAF^{V600E} kinase, including vemurafenib, dabrafenib and encorafenib, are the predominant targeted kinase therapies used to treat *BRAF^{V600E}* positive melanomas, but frequently result in widespread treatment resistance[63]. We FACS-isolated Low^{BRN2} and High^{BRN2} 624-mel cells and conducted vemurafenib response studies. We first used ptychography coupled with fluorescence microscopy to track the accumulation of cell mass over time – a sensitive readout of changes in cell growth in response to drug[64]. At high doses (1-10 μM) exposure to vemurafenib inhibited cell mass accumulation in both populations (**Fig. 5A**). Interestingly, at low concentrations (0.1 μM), we observed a paradoxical increase in mass accumulation exclusively in High^{BRN2} cells ($P < 0.0001$). We further noticed that in both populations, despite the decrease in mass accumulation at high doses, exposure to vemurafenib induced an increase in mCherry expression (**Fig. 5B-C**). At the population level, FACS-isolated Low^{BRN2} populations were more sensitive to the compound, exhibiting an IC50 of 0.26μM (95% CI: 0.15-0.45), consistent with the mass measurements (**Fig. 5D**). In contrast, the High^{BRN2} populations presented a more

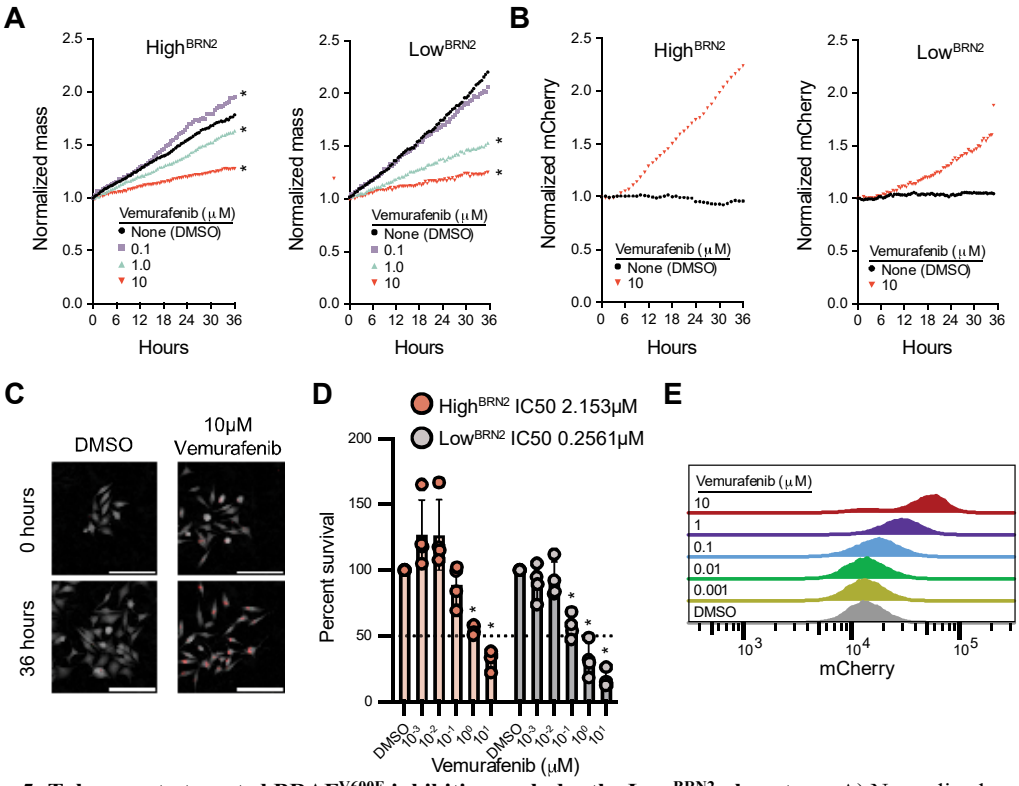

Figure 5: Tolerance to targeted BRAF^{V600E} inhibition excludes the Low^{BRN2} phenotype. A) Normalized mean single cell mass over time of FACS-enriched High^{BRN2} (left) and Low^{BRN2} (right) 624-mel cells exposed to indicated concentrations of vemurafenib. Asterisk indicates slopes significantly different from DMSO condition ($P < 0.0005$, simple linear regression). B) Normalized mean integrated mCherry intensity over time of FACS-enriched High^{BRN2} (left) and Low^{BRN2} (right) 624-mel cells exposed to indicated concentrations of vemurafenib. C) Representative image of Low^{BRN2} cells from B. Scale bar = 200μmt. D) Percent surviving cells after 48 hours of exposure to indicated concentrations of vemurafenib relative to DMSO condition. Asterisk indicates means significantly different from DMSO condition ($P < 0.0005$, unpaired T test). E) Flow analysis of mCherry expression from 624-mel reporter cells after 48 hours treatment with the indicated concentrations of vemurafenib.

complex response to vemurafenib. Specifically, at low doses (0.001-0.010 μM) vemurafenib again induced a minor, but non-significant, increase in cell number over 36 hours of treatment (**Fig. 5D**). At higher doses the High^{BRN2} populations exhibited an IC50 almost 10-fold higher than that of Low^{BRN2} cells (2.15μM, 95% CI: 0.73-6.37, $P < 0.0005$, unpaired t test). Flow analysis confirmed that exposure to vemurafenib induced a phenotype transition, such that all surviving cells uniformly expressed increased mCherry, thus depleting the population of Low^{BRN2} cells (**Fig. 5E**). Coupled with the observed necessity of the Low^{BRN2} state for graft efficiency (**Fig. 4**), our experiments demonstrate that BRAF^{V600E}-driven melanoma cells interconvert between two mutually exclusive and inheritable states – each of which promotes a distinct behavior associated with aggressive disease.

BRN2-associated drug-tolerant and tumorigenic phenotypes are present in human melanoma

We performed single-cell RNA sequencing (scRNAseq) on FACS-isolated Low^{BRN2} and High^{BRN2} 624-mel cells to explore the similarity and differences of individual cells within each population. Uniform Manifold Approximation and Projection (UMAP) revealed that while Low^{BRN2} and High^{BRN2} generally clustered together, most cells assembled as a single large population (**Fig. 6A, Supplemental Figure S3A**). Seurat clustering subdivided the population into nineteen clusters, each with varying fractions of Low^{BRN2} and High^{BRN2} cells (**Fig. 6B,**

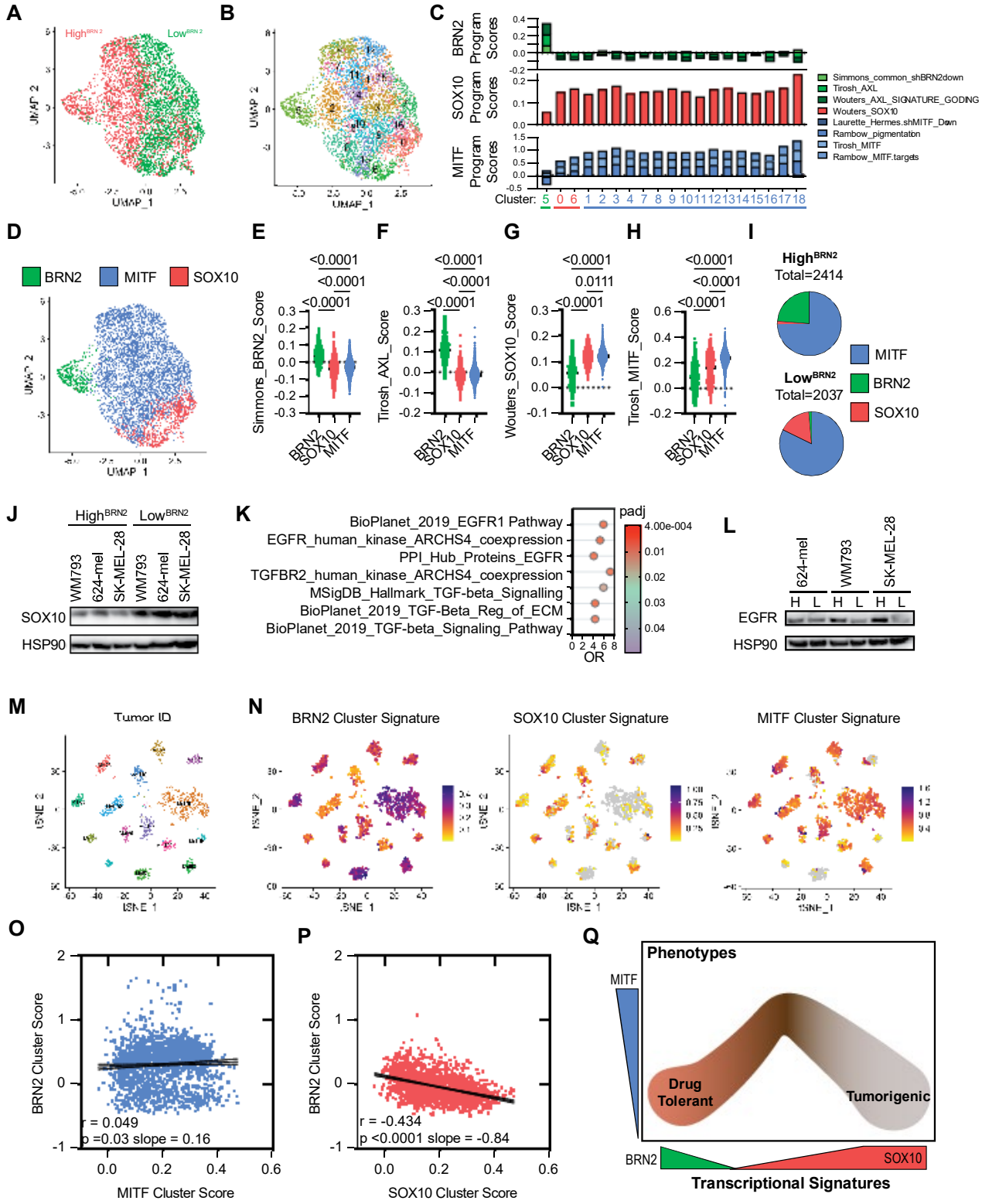

Supplemental Figure S3B). After examining previously published gene expression programs regulated by BRN2 and three other lineage-specific factors, MITF, AXL and SOX10, known for their roles in phenotype switching and targeted therapy response[17,34,35], we classified Seurat clusters into three groups (**Fig. 6C-D, Supplemental Figure S3C-D**). Cluster 5, composed of almost exclusively High^{BRN2} cells (**Supplemental Figure S3B**), had the highest expression of BRN2-regulated genes ("BRN2 genes")[26] and AXL-regulated genes ("AXL genes")[16] (**Fig. 6C,**

Figure 6: Distinct and mutually exclusive MITF low transcriptional states in human melanomas. A) Uniform manifold approximation and projection (UMAP) visualization of the 4,451 cells that passed quality control (Supplemental Fig. S3A), colored according to FACS enrichment ($High^{BRN2}$ or Low^{BRN2}). B) UMAP colored according to Seurat clustering (see also Supplemental Fig. S3B). C) ModuleScores for previously published BRN2 and AXL regulated genes (green); SOX10 regulated genes (red) and MITF regulated genes (blue). D) UMAP colored according to BRN2, SOX10, and MITF clusters. E-H) Distribution of gene signature scores within cells of the BRN2, NCSC, and MITF clusters (see also Supplemental Fig. S3C-D for UMAP representations of signature scores). P, ordinary one-way ANOVA. I) Pie charts indicating the percent of $High^{BRN2}$ and Low^{BRN2} cells from the BRN2, SOX10, and MITF clusters. J) Western blot analysis of SOX10 expression in FACS enriched mCherry high and mCherry low reporter cell lines. K) Gene set enrichment analysis (GSEA) comparing DE genes between $High^{BRN2}$ and Low^{BRN2} cells to signatures of known signaling pathways. L) Western blot analysis of EGFR expression in FACS enriched mCherry high and mCherry low reporter cell lines. M) tSNE plots of ex vivo human melanoma scRNAseq data from Jerby-Arnon, 2018. Tumor IDs identify unique patients. N) Scores for gene signatures unique to BRN2, SOX10, and MITF clusters are plotted as colorimetric onto tSNE plot from (M). O) MITF and N) SOX10 cluster scores versus BRN2 cluster scores for every cell in (M). Best-fit line, 95% CI from simple linear regression; r and p, Pearson correlation. N) Schematic summary of the relationship between observed transcriptional signatures (green, red, blue) and observed phenotypes (drug-tolerant and tumorigenic).

E, F) and so we refer to it as the BRN2 state (**Fig. 6D**, green). Notably, the BRN2 state exhibited poor expression of both SOX10-regulated genes ("SOX10 genes")[45] and MITF-regulated genes ("MITF genes")[16] (**Fig. 6C, E-H, Supplemental Figure S3C-D**). Conversely, clusters 0 and 6 were comprised mostly of Low^{BRN2} cells (**Supplemental Figure S3B)**, expressed less BRN2, AXL and MITF genes, but retained high expression of SOX10 genes (**Fig. 6C,E-H, Supplemental Figure S3C-D**), and so we refer to these as the SOX10 state (**Fig. 6D**, red). Finally, all other clusters, regardless of reporter status, expressed a similar pattern of uniformly highly expressed MITF genes, mediumly expressed SOX10 genes, and poorly expressed BRN2 and AXL genes (**Fig. 6C, E-H, Supplemental Figure S3C-D**), and instead differed from each other by cell cycle genes (**Supplemental Figure S3E-F**). We collectively refer to these as the MITF state (**Fig. 6D**, blue). We next examined the fractional composition of each group in the bulk population of Low^{BRN2} and $High^{BRN2}$ cells. As expected, BRN2 state cells were near-exclusive to the $High^{BRN2}$ population and SOX10 state cells were near-exclusive to the Low^{BRN2} (**Fig. 6I**). Consistent with these data, SOX10 protein expression was reduced in the $High^{BRN2}$ populations of all reporter lines (**Fig. 6J**). Our identification of a targeted therapy resistant SOX10 deficient population of melanoma cells, which exhibit relatively slower proliferation (**Fig. 2C**), is also consistent with previous reports[34,65]. Further validating the BRN2 state as the targeted therapy resistant cell state previously reported, this state was enriched for TGF-beta and EGFR gene expression programs (**Fig. 6K**) and bulk $High^{BRN2}$ cells expressed higher protein levels of EGFR relative to Low^{BRN2} cells (**Fig. 6L**).

We next aimed to ascertain if the triad of states delineated via scRNAseq and this reporter system were reflective of transcriptional conditions present within human tumors. For each cluster, we identified a distinct signature defined by a unique combination of differentially expressed genes (**Supplemental Table S2**). These distinct signatures were subsequently evaluated in a scRNAseq dataset encompassing fourteen *ex vivo* human melanoma tumors (**Fig. 6M**) generated by Tirosh et al[16] and Jerby-Arnon et al[66]. Consistent with previous reports, most tumors were comprised of cells heterogeneously expressing the MITF signature, the BRN2 signature, and/or the SOX10 signature (**Fig. 6N**)[14,16,34]. Interestingly, the BRN2 state signature was expressed in a largely bimodal manner – with distinct high and low expression states (**Fig. 6O**) not unlike the BRN2 promoter reporter expression pattern (**Fig. 1B**). While there was no obvious relationship between BRN2 and MITF state signature expression (**Fig. 6O**), the BRN2 and SOX10 states presented a significant anticorrelated expression pattern (**Fig. 6P**, $r = -0.434$, $p < 0.0001$). These findings

reinforce that the mutually exclusive transcriptional programs delineated in our reporter system aptly reflect the conditions present within human melanoma tumors.

Discussion

In this study, we used label-free live cell imaging coupled with a fluorescent reporter of BRN2 promoter activity to monitor the kinetics of phenotype switching in human melanoma cells in homeostatic conditions. Our work builds upon prior studies that either indirectly monitored phenotype switching by taking molecular snapshots at different time points or induced the switch through chemical, environmental, or genetic perturbation[21]. Through tracking individual live cells, we demonstrate phenotype heterogeneity within clonal populations that is re-established in standard culture conditions, as has been previously demonstrated for breast cancer and glioblastoma[67,68]. Switching occurs on an intermediate time scale, such that phenotypes are inherited through multiple generations while also undergoing spontaneous interconversion[69]. Transitions occurred both coupled with asymmetric division or independent of cell division. Since switching was bidirectional, our observations reinforce the dynamic stemness model in melanoma[1] where stem-like and non-tumorigenic cells reach a phenotypic equilibrium, potentially leading to unlimited tumorigenic potential if the stem-like state cannot be controlled. Further investigations into the underlying mechanisms that facilitate dynamic stemness and ways to prevent this transition are needed.

Pioneering work in this domain predicted that melanoma cells switched between two phenotypes – a MITF high and BRN2 low proliferative state and a MITF low and BRN2 high invasive state[15]. Our approach yielded observations consistent with recent studies that demonstrate a more complex phenotypic landscape within populations of melanoma cells[14,22,26,31,32,39,45]. Notably, we observed neither an obligatory relationship between BRN2 expression and migration nor evidence for a MITF-BRN2 axis. Instead, we observed two distinct MITF low transcriptional states characterized by the expression of either a BRN2- or a SOX10-regulated signature and associated with mutually exclusive phenotypes of drug tolerance and tumorigenicity (**Fig. 6Q**). The observed coexistence of these three states, within not only the isogenic and clonal homeostatic culture but also within human tumors, provides a plausible reconciliation for prior inconsistent findings in the field concerning the relationship between MITF and BRN2 programs. For instance, cultures classified as "MITF low" may actually constitute a blend of BRN2 and SOX10 states, with proportions potentially varying or even oscillating. In a similar vein, our data suggest that "SOX10 low" cultures are likely to exhibit a uniformity of low MITF levels, whereas "SOX10 high" cultures could encompass cells with a blend of high and low MITF. Further, this cell state heterogeneity in cultures and tumors would inevitably impact observed phenotypes, especially when only population means are considered. The two low MITF states, which reciprocally express BRN2 and SOX10, are likely akin to the BRN2 and NCSC states identified in earlier studies[1,14,31,34,70]. Consistently, SOX10 low melanoma cells (identified as $High^{BRN2}$ in this study) have been associated with increased tolerance to targeted therapy, whereas SOX10 high cells (Low^{BRN2} in this study) were depleted in drug-resistant tumors[14,34]. The mutual exclusivity of these two states, yet their individual contribution to different stages of melanoma progression (i.e., tumor initiation versus therapeutic resistance), offers a rational explanation for the paradoxical identification of BRN2 as both an oncogene and a tumor suppressor[8,23,33].

It is noteworthy that our single-cell phenotyping analysis suggested more uniformly discrete cell populations than what the scRNAseq analysis implied. This finding points towards the possibility that variations in the melanoma transcriptome, observed as distinct clusters in scRNAseq, do not invariably cause observed alterations in the phenome. This lack of supervenience of the transcriptome on the phenome aligns with both the broadly recognized general mismatch between transcript and protein expression[71,72], as well as the specific, complex layers of post-transcriptional regulation of MITF and BRN2[25]. It is also in line with the overarching phenomenon of biological robustness within cells[73,74]. This insight underscores the potential shortcomings of relying solely on scRNAseq to infer cell phenotypes. As strides are made toward characterizing distinct melanoma phenomes, the potential disconnect between the transcriptome and phenotype should be considered.

Prior studies have demonstrated that BRAF inhibitor-resistant cells also exhibit increased invasive or stem-like properties – linking the two deleterious phenotypes[70,75]. We were therefore surprised to identify distinct aggressive phenotypes associated with each mutually exclusive state. Our data suggest that once a melanoma is established, the induction of either state could progress the disease in discrete ways – increasing metastatic dissemination or decreasing therapeutic sensitivity. One limitation of our study is its reliance on melanoma cell lines for assaying phenotypes. Although we present evidence of both states existing within human tumors, we are unable to conclude that either state is associated with the same behaviors in situ as we observed in vitro and in vivo. We hypothesize that the burden of BRN2 state cells in patients' tumors could be predictive of the rate at which targeted therapy resistance occurs. Conversely, the percentage of SOX10 state cells could be prognostic of the likelihood of widespread dissemination or remission. The assembly of appropriate cohorts for assessing these hypotheses should be the subject of future investigation.

Overall, this research provides useful insights into the dynamics of phenotype switching in melanoma cells. Our findings highlight the importance of understanding the mechanisms underlying phenotypic switching in melanoma and the relationship between therapy-tolerant and stem-like tumorigenic properties. In particular, we emphasize the implications of our observations for strategies seeking to enhance the efficacy of melanoma therapies by targeting the mechanisms that control phenotype switching. As the induction of either phenotype could be detrimental to a patient, future studies should weigh the potential benefit of sensitizing cells to therapeutic regimens against the potential harm of increasing the risk of metastatic outgrowth.

Materials and Methods

Cell Culture Maintenance and Manipulation

Melanoma cell lines 624-Mel (CVCL_8054), SK-MEL-28 (CVCL_8054) and WM793 (CVCL_8787) were received as gifts from Dr. Boris Bastian and Dr. Meenhard Herlyn and were STR verified (**Supplemental Table S3**) and regularly monitored with the Universal Mycoplasma Detection Kit (ATCC 30-1012K). Cultures were maintained in RPMI1640 media (Thermo Fisher, 11-875-093) supplemented with 10% FBS (Corning, 35-010-CV), 1x penicillin-streptomycin, (Thermo Fisher, 15140122) and 2mM L-glutamine (UCSF core facility,

382 CCFGB002) at 37 °C, 5% CO_2. All cells were disassociated with 0.05% Trypsin EDTA
383 (Mediatech, MT 25-052-C1) followed by neutralization with equimolar soybean trypsin inhibitor
384 (Thermo Scientific, 17075029). The BRN2 reporter (pROM-POU3F2p-mCherry-Neo, Addgene
385 153321) was engineered by first inserting NLS-mCherry (Gift from Ron Vale, Addgene 67932)
386 and a pGK-driven neomycin resistance cassette into a 3rd generation vector backbone, pSicoR-
387 Ef1a-mCh-Puro, (Gift from Bruce Conklin, Addgene 31845)[76,77]. The BRN2 promoter was
388 amplified off of human DNA (**Supplementary Table S4**). Lenti-viral particles were generated as
389 previously described and transduced at MOI < 0.3 in the presence of 10 μg/mL polybrene (Sigma
390 TR-1003)[23]. Three days later, pROM-POU3F2p-mCherry-Neo transduced cells were selected
391 with neomycin (Sigma, A1720) for 3 weeks at the minimal concentration required for complete
392 toxicity of parental cells (cell line dependent, concentrations ranged from 100 μg/ml to 1000
393 μg/ml). Single cells from each selected culture were sorted using the SONY SH800 FACS
394 machine and expanded. Neomycin was periodically added to the media to ensure retention. For
395 isolation experiments, respective populations were FACS isolated twice in tandem followed by a
396 third analyses to ensure >99% purity. Flow analysis were conducted with a BD Fortessa.

397 *ATAC-Seq*

398 The ATAC-seq assay followed the published Omni-ATAC protocol[78]. Briefly, nuclei were
399 isolated from 50000 cells, which were then treated with 2.5ul of Tn5 transposase (Illumina
400 20034197) for DNA tagmentation. DNA was extracted and PCR amplified (5 cycles) using
401 barcoded primers that were included in the Omni-ATAC protocol[78]. The ATAC libraries were
402 sequenced by NovaSeq (50bp paired end). ATAC-sequenced reads were quality checked by
403 FastQC (v0.11.9), and then aligned to the human reference genome hg19 (GRCh37) using
404 Bowtie2 aligner (bowtie2-align-s version 2.4.2). Utilizing samtools (version 1.12), all
405 mitochondrial, unaligned, and low-quality reads (Q<20) and duplicated reads were filtered out,
406 and were then normalized for equal coverage in each group of cells. Removing adapters by
407 NGmerge (version 0.3), ATAC-enriched regions/peaks were identified by MACS (3.0.0a6) with
408 Q value cut off of 0.01 and with other default parameters. The identified peaks were visualized
409 through Integrated Genome Browser (IGB), and also were annotated by HOMER (v4.11.1-the
410 annotatePeaks.pl program). Finally, the differentially enriched peaks between two groups of cells
411 were evaluated via DiffBind (version 3.4.3), using DESeq2 method.

412 *Protein preparation and Western blotting*

413 At least 200,000 cells were lysed in RIPA buffer (Thermo 89901) containing a protease inhibitor
414 cocktail (Thermo 87785) and 0.5 M EDTA (Thermo 1861274), each used at 1:100 concentration,
415 incubated on ice for 10 minutes, then centrifuged at maximum speed for 20 minutes at 4°C. The
416 protein concentration of the supernatant was measure using the Pierce BCA protein assay kit
417 (Thermo 23225) and 10 μg of protein was loaded on a 4–12% Nupage bis-tris gel (Thermo
418 NP0323box), run for 2 hours at 130 V in running buffer (Novex NP0002), and dry-transferred
419 onto a nitrocellulose membrane (Biorad 1620115) using a Bio-Rad Trans-blot SD semi dry
420 transfer cell. The membrane was submerged in blocking buffer (Thermo, 37536) for 1 hour before
421 incubation with a primary antibody diluted in blocking buffer (**Supplemental Table S4**)
422 overnight, followed by trice washing in 0.2% Triton-X (Sigma T8787) in PBS before a secondary
423 antibody (Invitrogen G-21040 or Invitrogen G-21234, 1:2000) was added and incubated for 1
424 hour. After three washes, the membrane was imaged using an Azure Biosystem Imager. The
425 band intensity was measured by densitometry using Image J 1.52a.

426 *RNA preparation, and quantitative real-time PCR, bulk RNA sequencing*

427 FACS isolated cells were added to 0.5-1 mL of Trizol (Ambion 15596026) for RNA extraction
428 according to manufacturer's protocol. For qRT-PCR, cDNA from 0.5-1 μg of RNA (NanoDrop,

429 Thermo Scientific) was synthesized using the Sensifast synthesis kit (Bioline Bio-65053,
430 manufacturer's protocol) then diluted 1:5. Per RT-qPCR reaction, 1 µl of the dilution was mixed
431 with 0.41 µM primers (**Supplemental Table S4**) and 1x Sensifast SYBR non-Rox kit (Bioline
432 Bio98005). The real-time PCR program cycled as follows: one cycle of 95°C for 2 mins followed
433 by 40 cycles of 95°C for 5 seconds and 65°C for 30 seconds. For sequencing, intact poly(A)
434 RNA was purified from 100-500 ng of RNA (RIN 8-10, Agilent Technologies 2200 TapeStation)
435 with oligo(dT) magnetic beads and stranded mRNA sequencing libraries were prepared as
436 described using the Illumina TruSeq Stranded mRNA Library Prep kit (20020595) and TruSeq
437 RNA UD Indexes (20022371). Purified libraries were qualified on an Agilent Technologies 2200
438 TapeStation using a D1000 ScreenTape assay (cat# 5067-5582 and 5067-5583). The molarity of
439 adapter-modified molecules was defined by quantitative PCR using the Kapa Biosystems Kapa
440 Library Quant Kit (cat#KK4824). Sequencing libraries (1.3 nM) were chemically denatured and
441 applied to an Illumina NovaSeq flow cell using the NovaSeq XP chemistry workflow (20021664).
442 Following transfer of the flowcell to an Illumina NovaSeq instrument, a 2 x 51 cycle paired end
443 sequence run was performed using a NovaSeq S1 reagent Kit (20027465). Gene set enrichment
444 analyses were conducted as previously described[7].

445 *Single molecule RNA FISH*

446 smFISH experiments were conducted with in house reagents as previously described[79]. Briefly,
447 probes were developed using the designer tool from Stellaris (LGC Biosearch Technologies)
448 using a masking level of 5, a minimum of 2 base pair spacing between single probes, and a length
449 of 18 nt (**Supplemental Table S4**). Approximately $5x10^5$ disassociated cells were immobilized
450 on a Cell-Tak (Corning, CB-40240) coated 8-well chambered image dish, fixed with 5%
451 formaldehyde (Tousimis 1008A), 1X PBS for 10 minutes, washed with 1X PBS then stored in
452 70% EtOH at 4 °C for a minimum of one hour. Cells were then washed first with 2X SSC
453 (Thermo Fisher Scientific 15557044) containing 10% v/v deionized Formamide (Thermo Fisher
454 Scientific AM9342), then with hybridization buffer consisting of 10% w/w dextran sulfate (Sigma
455 Aldrich 42867) in 1X SSC with 10% v/v Formamide, and incubated overnight at 37 °C in
456 hybridization buffer containing 25 nM probes. Cells were then incubated for 30 minutes at 37 °C
457 in 2X SSC containing 10% v/v Formamide, followed by 15 minutes at 37 °C in 2X SSC
458 containing 10% v/v Formamide and DAPI (Thermo Fisher Scientific D1306). Finally, cells were
459 washes with 2X SSC and incubated for 2 min at room temperature in 2X SSC, 10% w/w glucose
460 (Sigma Aldrich G7021), 0.01 M Tris pH 8 (Life Technologies AM9855G). To minimize photo
461 bleaching, cells were imaged in a photo-protective buffer containing 2X SSC, 10% w/w glucose,
462 0.01 M Tris pH 8, 75 µg/mL glucose oxidase (Sigma Aldrich G0543-10K), 520 µg/mL catalase
463 (Sigma Aldrich C3156-50), and 0.5 mg/mL Trolox (Sigma Aldrich 238813). Images were taken
464 with a Nikon Ti-E microscope equipped with a W1 Spinning Disk unit, an Andor iXon Ultra
465 DU888 1k x 1k EMCCD camera and a Plan Apo VC 100x/1.4 oil objective in the UCSF Nikon
466 Imaging Center. Approximately 10 xy locations were randomly selected for each condition, and
467 analyzed using Fiji and in-house programs[79,80].

468 *Quantitative Immunofluorescence*

469 Cells were fixed in 4% paraformaldehyde (PFA) in PBS (Biotium 22023) for 15 minutes at room
470 temperature followed by pre-cooled (-20°C) methanol for 10 min at -20°C. Cells where thrice
471 washed in PBS then incubated in blocking buffer (5% Donkey Serum (Jackson Immuno Research
472 Labs 017-000-121, 1% BSA (Sigma A9647), 0.1% Triton X-100 (Sigma T8787) in PBS) for one
473 hour at room temperature. Cells were incubated at 4°C overnight with anti-BRN2 (Cell Signaling
474 12137S, 1:1000), thrice washed in PBS and incubated at room temperature for 1 hour with goat
475 anti-rabbit Alexa Fluor Plus 488 (Invitrogen, A32731, 1:10000). Cells were washed, incubated
476 with DAPI (Thermo Fisher D1306, 1:1000) for 5 min at room temperature, washed twice more
477 and imaged using the INCell Analyzer 2000 high throughput high content imager (GE).

478 *Quantitative Phase Imaging to Assess Proliferation, Motility, Morphology and Reporter*
479 *Fluorescence*

480 100,000 cells were seeded per well of a standard tissue-culture treated 6-well polystyrene plate
481 (Sarstedt 83.3920.005) for digital holographic cytometry (DHC) using the M4 Holomonitor
482 (Phase Holographic Imaging, Sweden). Cells were monitored for 72 hours. Morphology was
483 analyzed using the HStudio Software and linear discriminant analysis as previously described[55–
484 57]. For Fourier pthychography coupled to fluorescent microscopy, 1,200 cells were seeded per
485 well of a standard-culture treated 96-well plate then imaged with the LiveCyte (Phasefocus,
486 United Kingdom) every 30 minutes for 48-72 hours. Proliferation and motility were analyzed
487 using the Analysis dashboards provided by the manufacturer. Cell mass was calculated by
488 segmenting cell objects from background using Sobel edge detection thresholding, then summing
489 the phase shift relative to background over all object (cell) pixels, and assuming a specific
490 refractive increment of 1.8×10^{-4} m^3/kg[64]. Cell lineages were visualized using a customized
491 software based on Loon[81].

492 *Engraftment Efficiency Assay*

493 All protocols described in this and other sections regarding animal studies were approved by the
494 UCSF Institutional Animal Care and Use Committee. Ethical endpoint for tumor transplantation
495 experiments was reached when a tumor was 2.5 cm or more in any single dimension. Human
496 melanoma cell lines with fluorescent BRN2 reporter were further transduced with pHIV-Luc-
497 ZsGreen (Addgene 39196) and selected with neomycin (800 µg/mL) for 3 weeks. GFP high
498 expressing cells were isolated by FACS and expanded. mCherry reporter high and reporter low
499 cells were then FACS isolated as described above. 2 million cells from each group were injected
500 into the flank of adult male NOD *scid* gamma mice at a site distant from the lungs. Mice were
501 imaged in a PerkinElmer IVIS Spectrum Imaging System for luminescence every 2 weeks, 15
502 minutes after subcutaneous injection of 100 µl (150 mg Luciferin/kg body weight) of D-luciferin
503 (Goldbio LUCK-1G). After the final week, mice were immediately sacrificed and organs were
504 harvested and imaged. All animal studies were conducted by the UCSF Preclinical Therapeutics
505 Core, of which the technicians were blinded to the cell types and hypotheses. Each group initially
506 contained seven mice.

507 *Single Cell RNA Sequencing*

508 scRNASeq libraries were prepared from freshly disassociated cell cultures according the BD
509 Rhapsody System mRNA Whole Transcriptome Analysis manufacturer's protocol (selected
510 parameters: 11 cycles for sample tag PCR1 and 13 cycles for RPE PCR) and sequenced on an S4
511 Flow Cell of a NovaSeq6000. Raw data were processed using the BD Rhapsody WTA Analysis
512 pipeline (https://igor.sbgenomics.com/public/apps/jiewho/bd-public-project/bd-rhapsody-wta-
513 analysis-pipeline) which generates BAM files and single count matrices from raw FASTQ files.
514 The BD Rhapsody output files (RSEC_MolsPerCell and Sample_Tag_Calls) were loaded into the
515 Seurat 4.2.0 package in R[82]. Cells from 624Mel mcherry low and high were normalized using the
516 sctransform v2 method[83] and clustered using 15 dimensions and a 2.0 resolution with UMAP.
517 Differentially expressed genes were identified using the default Wilcoxon Rank Sum test in
518 Seurat. A gene set signature score was calculated for each cell by dividing the number of
519 expressed genes in the set (with 1 or more read) by the total number of genes in the set. Module
520 scores were added using `AddModuleScore` in Seurat to identity gene sets with higher or lower
521 expression than a random set of 100 genes[16]. Cell cycle scores were calculated using
522 `CellCycleScoring` in Seurat with the 2019 update of cell cycle genes. The cell annotations and
523 count files from Jerby-Arnon et al[66] were downloaded from GSE115978 at NCBI GEO and then
524 combined into a Seurat object. The counts were normalized using the global-scaling
525 normalization and module scores were added using AddModuleScore. The tSNE coordinates

526 from the Single-cell portal (SCP109 Melanoma immunotherapy resistance) were added to the
527 object for plotting module scores.

528 *Data Availability*

529 The mRNA-sequencing data produced in this manuscript is available from GEO (GSE150582 and
530 GSE230574).

531 *Statistical Analyses*

532 For differential gene expression, p values were calculated with the DESeq2 (v1.30.1) default
533 Wald test adjusted by the Benjamini-Hochberg method using a 5% false discovery rate (FDR)[84].
534 Pathway analyses were analyzed using the fast gene set enrichment package in R with a 10%
535 FDR[85]. Gene set enrichment analyses were conducted using GSEA (v4.0.3, Broad Institute)
536 Preranked tool with 1000 permutations. For other experiments, unpaired t-tests were used for
537 Gaussian distributions and Mann-Whitney tests for non-Gaussian distributions or for samples of
538 unequal variance. Exact p values were calculated as reported by Prism 8 (Graphpad).
539

540 **References**

541 1. Arozarena, I. & Wellbrock, C. Phenotype plasticity as enabler of melanoma progression
542 and therapy resistance. *Nature Reviews Cancer* vol. 19 377–391 Preprint at
543 https://doi.org/10.1038/s41568-019-0154-4 (2019).

544 2. Tang, Y., Durand, S., Dalle, S. & Caramel, J. EMT-Inducing Transcription Factors,
545 Drivers of Melanoma Phenotype Switching, and Resistance to Treatment. *Cancers* **12**, 1–17
546 (2020).

547 3. Landsberg, J. *et al.* Melanomas resist T-cell therapy through inflammation-induced
548 reversible dedifferentiation. *Nature* **490**, 412–416 (2012).

549 4. Seip, K. *et al.* Fibroblast-induced switching to the mesenchymal-like phenotype and
550 PI3K/mTOR signaling protects melanoma cells from BRAF inhibitors. *Oncotarget* **7**, 19997–
551 20015 (2016).

552 5. Caramel, J. *et al.* A Switch in the Expression of Embryonic EMT-Inducers Drives the
553 Development of Malignant Melanoma. *Cancer Cell* **24**, 466–480 (2013).

554 6. Konieczkowski, D. J. *et al.* A melanoma cell state distinction influences sensitivity to
555 MAPK pathway inhibitors. *Cancer Discovery* **4**, (2014).

556 7. McNeal, A. S. *et al.* Brafv600e induces reversible mitotic arrest in human melanocytes via
557 microrna-mediated suppression of aurkb. *eLife* **10**, (2021).

558 8. Pinner, S. *et al.* Intravital imaging reveals transient changes in pigment production and
559 Brn2 expression during metastatic melanoma dissemination. *Cancer research* **69**, 7969–77
560 (2009).

561 9. Falletta, P. *et al.* Translation reprogramming is an evolutionarily conserved driver of
562 phenotypic plasticity and therapeutic resistance in melanoma. *Genes & Development* **31**, 18–
563 33 (2017).

564 10. Kim, I. S. *et al.* Microenvironment-derived factors driving metastatic plasticity in
565 melanoma. *Nature Communications 2017 8:1* **8**, 1–11 (2017).

566 11. Hoek, K. S. *et al.* In vivo Switching of Human Melanoma Cells between Proliferative and
567 Invasive States. *Cancer Research* **68**, 650–656 (2008).

12. Hoek, K. S. & Goding, C. R. Cancer stem cells versus phenotype-switching in melanoma. *Pigment Cell & Melanoma Research* **23**, 746–759 (2010).

13. Tsoi, J. *et al.* Multi-stage Differentiation Defines Melanoma Subtypes with Differential Vulnerability to Drug-Induced Iron-Dependent Oxidative Stress. *Cancer Cell* **33**, (2018).

14. Rambow, F. *et al.* Toward Minimal Residual Disease-Directed Therapy in Melanoma. *Cell* **174**, 843-855.e19 (2018).

15. Widmer, D. S. *et al.* Systematic classification of melanoma cells by phenotype-specific gene expression mapping. *Pigment Cell & Melanoma Research* **25**, 343–353 (2012).

16. Tirosh, I. *et al.* Dissecting the multicellular ecosystem of metastatic melanoma by single-cell RNA-seq. *Science* **352**, 189–196 (2016).

17. Müller, J. *et al.* Low MITF/AXL ratio predicts early resistance to multiple targeted drugs in melanoma. *Nature Communications* **5**, (2014).

18. Wellbrock, C. & Arozarena, I. Microphthalmia-associated transcription factor in melanoma development and MAP-kinase pathway targeted therapy. *Pigment Cell and Melanoma Research* **28**, (2015).

19. Bittner, M. *et al.* Molecular classification of cutaneous malignant melanoma by gene expression profiling. *Nature* **406**, 536–540 (2000).

20. Cook, A. L., Boyle, G. M., Leonard, J. H., Parsons, P. G. & Sturm, R. A. BRN2 in melanocytic cell development, differentiation, and transformation. in *From Melanocytes to Melanoma: The Progression to Malignancy* 149–167 (Humana Press, 2006).

21. Fane, M. E., Chhabra, Y., Smith, A. G. & Sturm, R. A. BRN2, a POUerful driver of melanoma phenotype switching and metastasis. *Pigment Cell and Melanoma Research* vol. 32 9–24 Preprint at https://doi.org/10.1111/pcmr.12710 (2019).

22. Chitsazan, A. *et al.* Unexpected High Levels of BRN2/POU3F2 Expression in Human Dermal Melanocytic Nevi. *Journal of Investigative Dermatology* **140**, (2020).

23. Zeng, H. *et al.* Bi-allelic Loss of CDKN2A Initiates Melanoma Invasion via BRN2 Activation Article Bi-allelic Loss of CDKN2A Initiates Melanoma Invasion via BRN2 Activation. *Cancer Cell* **34**, 56-68.e9 (2018).

24. Lüönd, F. *et al.* Hierarchy of TGFβ/SMAD, Hippo/YAP/TAZ, and Wnt/ β-catenin signaling in melanoma phenotype switching. *Life Science Alliance* **5**, (2022).

25. Boyle, G. M. *et al.* Melanoma cell invasiveness is regulated by miR-211 suppression of the BRN2 transcription factor. *Pigment Cell & Melanoma Research* **24**, 525–537 (2011).

26. Simmons, J. L., Pierce, C. J., Al-Ejeh, F. & Boyle, G. M. MITF and BRN2 contribute to metastatic growth after dissemination of melanoma. *Scientific Reports* **7**, 10909 (2017).

27. Thurber, A. E. *et al.* Inverse expression states of the BRN2 and MITF transcription factors in melanoma spheres and tumour xenografts regulate the NOTCH pathway. *Oncogene* **30**, 3036–3048 (2011).

28. Wellbrock, C. *et al.* Oncogenic BRAF regulates melanoma proliferation through the lineage specific factor MITF. *PLoS ONE* **3**, (2008).

29. Goodall, J. *et al.* Brn-2 represses microphthalmia-associated transcription factor expression and marks a distinct subpopulation of microphthalmia-associated transcription factor-negative melanoma cells. *Cancer research* **68**, 7788–94 (2008).

610 30. Thomson, J. *et al.* The brn-2 gene regulates the melanocytic phenotype and tumorigenic
611 potential of human melanoma cells. *Oncogene* **11**, 691–700 (1995).

612 31. Smith, M. P. *et al.* A PAX3/BRN2 rheostat controls the dynamics of BRAF mediated
613 MITF regulation in MITFhigh/AXLlow melanoma. *Pigment Cell and Melanoma Research*
614 **32**, 280–291 (2019).

615 32. Simmons, J. L., Neuendorf, H. M. & Boyle, G. M. BRN2 and MITF together impact AXL
616 expression in melanoma. *Experimental Dermatology* **31**, (2022).

617 33. Hamm, M. *et al.* BRN2 is a non-canonical melanoma tumor-suppressor. *Nature*
618 *Communications* **12**, (2021).

619 34. Capparelli, C. *et al.* Targeting SOX10-deficient cells to reduce the dormant-invasive
620 phenotype state in melanoma. *Nat Commun* **13**, 1381 (2022).

621 35. Goding, C. R. & Arnheiter, H. MITF—the first 25 years. *Genes Dev.* **33**, 983–1007
622 (2019).

623 36. Bondurand, N. Interaction among SOX10, PAX3 and MITF, three genes altered in
624 Waardenburg syndrome. *Human Molecular Genetics* **9**, 1907–1917 (2000).

625 37. Lai, X. *et al.* SOX10 ablation severely impairs the generation of postmigratory neural
626 crest from human pluripotent stem cells. *Cell Death Dis* **12**, 814 (2021).

627 38. Tang, Y. & Cao, Y. SOX10 Knockdown Inhibits Melanoma Cell Proliferation via Notch
628 Signaling Pathway. *CMAR* **Volume 13**, 7225–7234 (2021).

629 39. Haass, N. K. *et al.* Real-time cell cycle imaging during melanoma growth, invasion, and
630 drug response. *Pigment Cell Melanoma Res.* **27**, 764–776 (2014).

631 40. Gay, C. M., Balaji, K. & Byers, L. A. Giving AXL the axe: targeting AXL in human
632 malignancy. *Br J Cancer* **116**, 415–423 (2017).

633 41. Jeter, J. M. *et al.* Chemoprevention agents for melanoma: A path forward into phase 3
634 clinical trials. *Cancer* **125**, 18–44 (2019).

635 42. Sáez-Ayala, M. *et al.* Directed Phenotype Switching as an Effective Antimelanoma
636 Strategy. *Cancer Cell* **24**, 105–119 (2013).

637 43. Smith, M. P. *et al.* Inhibiting Drivers of Non-mutational Drug Tolerance Is a Salvage
638 Strategy for Targeted Melanoma Therapy. *Cancer Cell* **29**, 270–284 (2016).

639 44. Benboubker, V., Boivin, F., Dalle, S. & Caramel, J. Cancer Cell Phenotype Plasticity as a
640 Driver of Immune Escape in Melanoma. *Front. Immunol.* **13**, 873116 (2022).

641 45. Wouters, J. *et al.* Robust gene expression programs underlie recurrent cell states and
642 phenotype switching in melanoma. *Nat Cell Biol* **22**, 986–998 (2020).

643 46. Monzani, E. *et al.* Melanoma contains CD133 and ABCG2 positive cells with enhanced
644 tumourigenic potential. *European Journal of Cancer* **43**, 935–946 (2007).

645 47. Madjd, Z. *et al.* Expression of CD133 cancer stem cell marker in melanoma: A systematic
646 review and meta-analysis. *International Journal of Biological Markers* vol. 31 e118–e125
647 Preprint at https://doi.org/10.5301/jbm.5000209 (2016).

648 48. Quintana, E. *et al.* Phenotypic Heterogeneity among Tumorigenic Melanoma Cells from
649 Patients that Is Reversible and Not Hierarchically Organized. *Cancer Cell* **18**, 510–523
650 (2010).

651 49. Morita, S. *et al.* Humanized anti-CD271 monoclonal antibody exerts an anti-tumor effect
652 by depleting cancer stem cells. *Cancer letters* (2019) doi:10.1016/j.canlet.2019.07.011.

653 50. Boiko, A. D. *et al.* Human melanoma-initiating cells express neural crest nerve growth
654 factor receptor CD271. *Nature* **466**, 133–137 (2010).

655 51. Civenni, G. *et al.* Human CD271-positive melanoma stem cells associated with metastasis
656 establish tumor heterogeneity and long-term growth. *Cancer Research* **71**, 3098–3109 (2011).

657 52. Boyle, S. E. *et al.* CD271 Expression on Patient Melanoma Cells Is Unstable and
658 Unlinked to Tumorigenicity. *Cancer Research* **76**, 3965–3977 (2016).

659 53. Cheli, Y. *et al.* CD271 is an imperfect marker for melanoma initiating cells. *Oncotarget* **5**,
660 5272–83 (2014).

661 54. Quintana, E. *et al.* Efficient tumour formation by single human melanoma cells. *Nature*
662 **456**, 593–8 (2008).

663 55. Hejna, M., Jorapur, A., Song, J. S. & Judson, R. L. High accuracy label-free classification
664 of single-cell kinetic states from holographic cytometry of human melanoma cells. *Scientific*
665 *Reports* **7**, (2017).

666 56. Zhang, Y. & Judson, R. L. Evaluation of holographic imaging cytometer holomonitor
667 M4® motility applications. *Cytometry Part A* **93**, 1125–1131 (2018).

668 57. Barker, K. L., Boucher, K. M. & Judson-Torres, R. L. Label-Free Classification of
669 Apoptosis, Ferroptosis and Necroptosis Using Digital Holographic Cytometry. *Applied*
670 *Sciences* **10**, 4439 (2020).

671 58. Liberzon, A. *et al.* The Molecular Signatures Database Hallmark Gene Set Collection.
672 *Cell Systems* **1**, 417–425 (2015).

673 59. Belote, R. L. *et al.* Human melanocyte development and melanoma dedifferentiation at
674 single-cell resolution. *Nature Cell Biology 2021 23:9* **23**, 1035–1047 (2021).

675 60. Marrison, J., Räty, L., Marriott, P. & O'Toole, P. Ptychography – a label free, high-
676 contrast imaging technique for live cells using quantitative phase information. *Sci Rep* **3**, 2369
677 (2013).

678 61. Einarsdottir, B. O. *et al.* Melanoma patient-derived xenografts accurately model the
679 disease and develop fast enough to guide treatment decisions. *Oncotarget* **5**, 9609–9618
680 (2014).

681 62. Cancer Genome Atlas Network. Genomic Classification of Cutaneous Melanoma. *Cell*
682 **161**, 1681–1696 (2015).

683 63. Sullivan, R. J. & Flaherty, K. T. Resistance to BRAF-targeted therapy in melanoma. *Eur J*
684 *Cancer* **49**, 1297–1304 (2013).

685 64. Zangle, T. A. & Teitell, M. A. Live-cell mass profiling: an emerging approach in
686 quantitative biophysics. *Nat Methods* **11**, 1221–1228 (2014).

687 65. Sun, C. *et al.* Reversible and adaptive resistance to BRAF(V600E) inhibition in
688 melanoma. *Nature* **508**, 118–122 (2014).

689 66. Jerby-Arnon, L. *et al.* A Cancer Cell Program Promotes T Cell Exclusion and Resistance
690 to Checkpoint Blockade. *Cell* **175**, 984-997.e24 (2018).

691 67. Gupta, P. B. *et al.* Stochastic State Transitions Give Rise to Phenotypic Equilibrium in
692 Populations of Cancer Cells. *Cell* **146**, 633–644 (2011).

68. Neftel, C. *et al.* An Integrative Model of Cellular States, Plasticity, and Genetics for Glioblastoma. *Cell* **178**, 835-849.e21 (2019).

69. Shaffer, S. M. *et al.* Rare cell variability and drug-induced reprogramming as a mode of cancer drug resistance. *Nature* **546**, 431–435 (2017).

70. Rambow, F., Marine, J.-C. & Goding, C. R. Melanoma plasticity and phenotypic diversity: therapeutic barriers and opportunities. *Genes Dev.* **33**, 1295–1318 (2019).

71. Vogel, C. & Marcotte, E. M. Insights into the regulation of protein abundance from proteomic and transcriptomic analyses. *Nat Rev Genet* **13**, 227–232 (2012).

72. Schwanhäusser, B. *et al.* Global quantification of mammalian gene expression control. *Nature* **473**, 337–342 (2011).

73. Ebert, M. S. & Sharp, P. A. Roles for MicroRNAs in Conferring Robustness to Biological Processes. *Cell* **149**, 515–524 (2012).

74. Vand-Rajabpour, F., Savage, M., Belote, R. L. & Judson-Torres, R. L. Critical Considerations for Investigating MicroRNAs during Tumorigenesis: A Case Study in Conceptual and Contextual Nuances of miR-211-5p in Melanoma. *Epigenomes* **7**, 9 (2023).

75. Arozarena, I. & Wellbrock, C. Targeting invasive properties of melanoma cells. *FEBS J* **284**, 2148–2162 (2017).

76. Tanenbaum, M. E., Stern-Ginossar, N., Weissman, J. S. & Vale, R. D. Regulation of mRNA translation during mitosis. *eLife* **4**, (2015).

77. Salomonis, N. *et al.* Alternative splicing regulates mouse embryonic stem cell pluripotency and differentiation. *Proceedings of the National Academy of Sciences* **107**, 10514–10519 (2010).

78. Corces, M. R. *et al.* An improved ATAC-seq protocol reduces background and enables interrogation of frozen tissues. *Nature Methods* **14**, (2017).

79. Hansen, M. M. K. *et al.* A Post-Transcriptional Feedback Mechanism for Noise Suppression and Fate Stabilization. *Cell* **173**, 1609-1621.e15 (2018).

80. Schindelin, J. *et al.* Fiji: an open-source platform for biological-image analysis. *Nature Methods* **9**, 676–682 (2012).

81. Lange, D., Polanco, E., Judson-Torres, R., Zangle, T. & Lex, A. Loon: Using Exemplars to Visualize Large-Scale Microscopy Data. *IEEE Trans Vis Comput Graph* **28**, 248–258 (2022).

82. Satija, R., Farrell, J. A., Gennert, D., Schier, A. F. & Regev, A. Spatial reconstruction of single-cell gene expression data. *Nat Biotechnol* **33**, 495–502 (2015).

83. Hafemeister, C. & Satija, R. Normalization and variance stabilization of single-cell RNA-seq data using regularized negative binomial regression. *Genome Biol* **20**, 296 (2019).

84. Benjamini, Y., Drai, D., Elmer, G., Kafkafi, N. & Golani, I. Controlling the false discovery rate in behavior genetics research. in *Behavioural Brain Research* vol. 125 (2001).

85. Korotkevich, G. *et al.* Fast gene set enrichment analysis. *bioRxiv* 060012 (2021) doi:10.1101/060012.

Acknowledgments

We utilized the Shared Resources for Research Informatics, High-Throughput Genomics and Bioinformatics Analysis, Preclinical Research, and Flow Cytometry and received direct financial support for the research reported in this publication provided by the Cell Response and Regulation Program at Huntsman Cancer Institute at the University of Utah, each supported by the National Cancer Institute of the National Institutes of Health under Award Number P30CA042014. The content is solely the responsibility of the authors and does not necessarily represent the official views of the NIH or other funding agencies.

Funding:
This work was supported by the Department of Defense Melanoma Research Program (W81XWH2010530 awarded to DG, MWV, and RLJ and W81XWH2210495 awarded to RLB), the National Institutes of Health Director's Common Fund (DP5 OD019787 to RLJ), 5 for the Fight Fellowship (to RLJ), and the Elsa U. Pardee Foundation (CA-0122861 to YZ). Effort for RLJ was supported by the UCSF Program for Breakthrough Biomedical Research Sandler Fellowship and the National Cancer Institute (R01CA229896 to RLJ). We acknowledge the direct financial support for the research reported in this publication provided the University of Utah's 1U4U seed grants.

Author contributions:

Conceptualization: YZ, RLJT; Methodology: YZ, RLB, TZ; Software: DL; Validation: MU; Formal analysis: RLB, MMKH, MH, TEM, FVR, MC, BKL, CS, XZ, TZ, RLJT; Investigation: YZ, RLB, MU, MMKH, TL, XZ, RLJT; Resources: RLJT; Data Curation: RLB, MC, CS, RLJT; Writing – Original Draft: RLJT; Writing – Review & Editing: YZ, RLB, MU, MMKH, FVR, RK; Visualization: RLB, MU, FVR, CS, TZ, RLJT; Supervision: AL, LSW, RK, RLJT; Project administration: RLJT; Funding acquisition: YZ, MWV, DG, RLJT

Competing interests:

The authors have no competing interests to declare.

Data and materials availability:

All data are available in the main text or the supplementary materials. The mRNA-sequencing data produced in this manuscript is available from GEO (GSE150582 and GSE230574).

Supplementary Materials

Supplemental Figure S1: Flow analysis of clonally expanded and serially cultured reporter cells. Flow analysis of clonally expanded then serially cultured SK-MEL-28 and WM793 cells with the BRN2 reporter.

Supplemental Figure S2: Generation of horizon charts. Graphical depiction of how the horizon charts portrayed in Fig. 3C are generated.

Supplemental Figure S3: Quality control metrics for single cell sequencing.

A) Percent of mitochondrial transcripts (pct_MT) and number of unique genes (nFeature_RNA) for single cell sequencing data. B) Representation of $High^{BRN2}$ and Low^{BRN2} cells in each Seurat cluster. C-D) UMAP representations of signature scores for BRN2, AXL, MITF, and SOX10

780 regulated genes. E) UMAP with each cell colored by predicted cell cycle phase. F) The percent of
781 cells in each Seurat cluster predicted in cell cycle phase.

782

783 **Supplemental Videos S1-2: Time-lapse imaging capturing bidirectional phenotype**
784 **switching.**
785
786 **Supplemental Table S1: Differential expression analysis from bulk sequencing of mCherry**
787 **high and low 624Mel cells.**
788
789 **Supplemental Table S2: Differential expression analysis from single cell sequencing of**
790 **mCherry high and low 624Mel cells.**
791
792 **Supplemental Table S3: STR analysis of cell lines used in study.**
793
794 **Supplemental Table S4: Reagents used in study**.

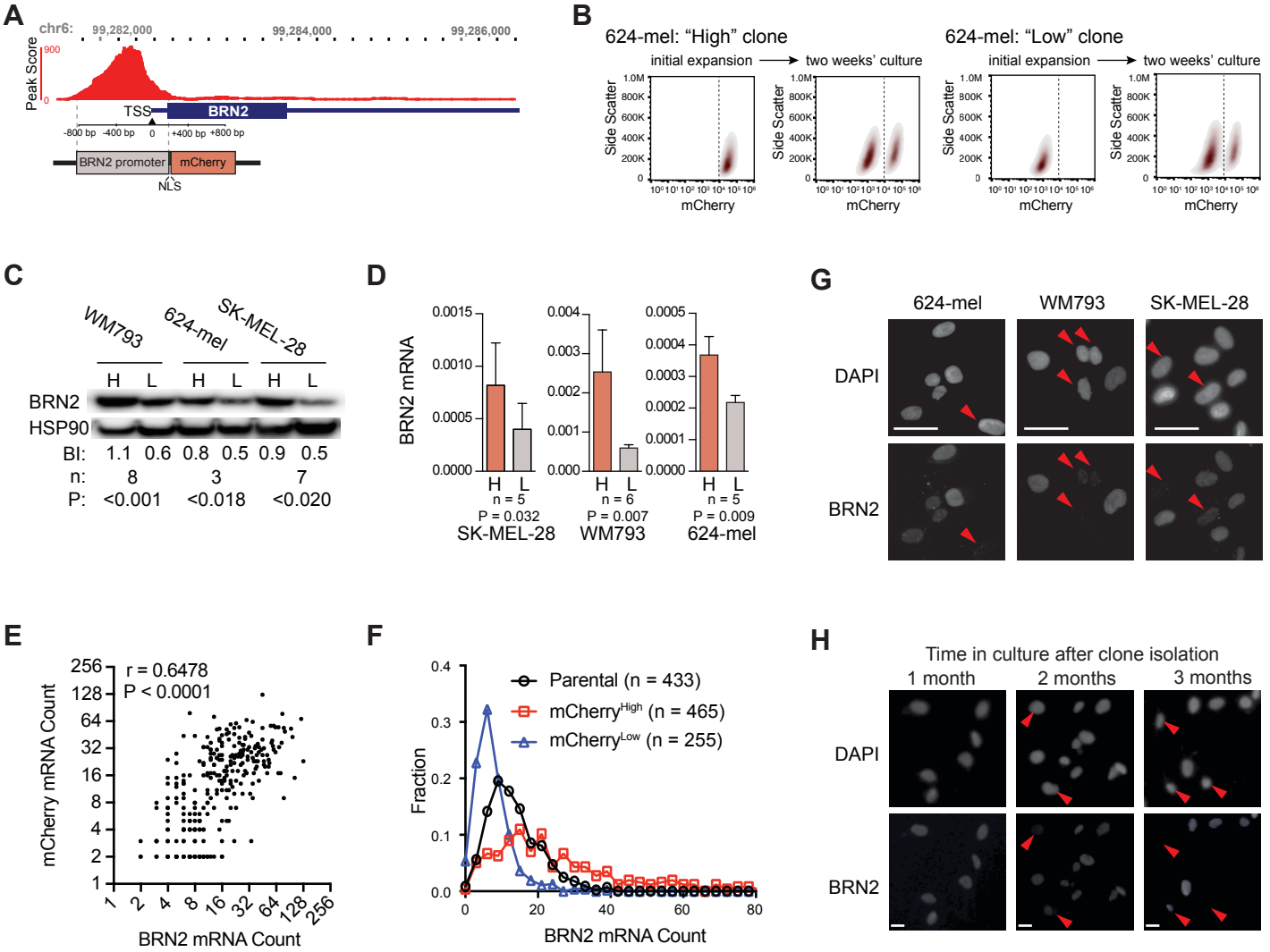
A
chr6:
99,282,000
99,284,000
99,286,000
Peak Score
900
0
TSS
BRN2
-800 bp
-400 bp
0
+400 bp
+800 bp
BRN2 promoter
mCherry
NLS
B
624-mel: "High" clone
initial expansion
two weeks' culture
624-mel: "Low" clone
Side Scatter
mCherry
C
WM793
624-mel
SK-MEL-28
H
L
BRN2
HSP90
BI: 1.1 0.6 0.8 0.5 0.9 0.5
n: 8 3 7
P: <0.001 <0.018 <0.020
D
BRN2 mRNA
n = 5
P = 0.032
SK-MEL-28
n = 6
P = 0.007
WM793
n = 5
P = 0.009
624-mel
G
624-mel
WM793
SK-MEL-28
DAPI
BRN2
E
r = 0.6478
P < 0.0001
mCherry mRNA Count
BRN2 mRNA Count
F
Parental (n = 433)
mCherryHigh (n = 465)
mCherryLow (n = 255)
Fraction
BRN2 mRNA Count
H
Time in culture after clone isolation
1 month
2 months
3 months
DAPI
BRN2

Figure 1

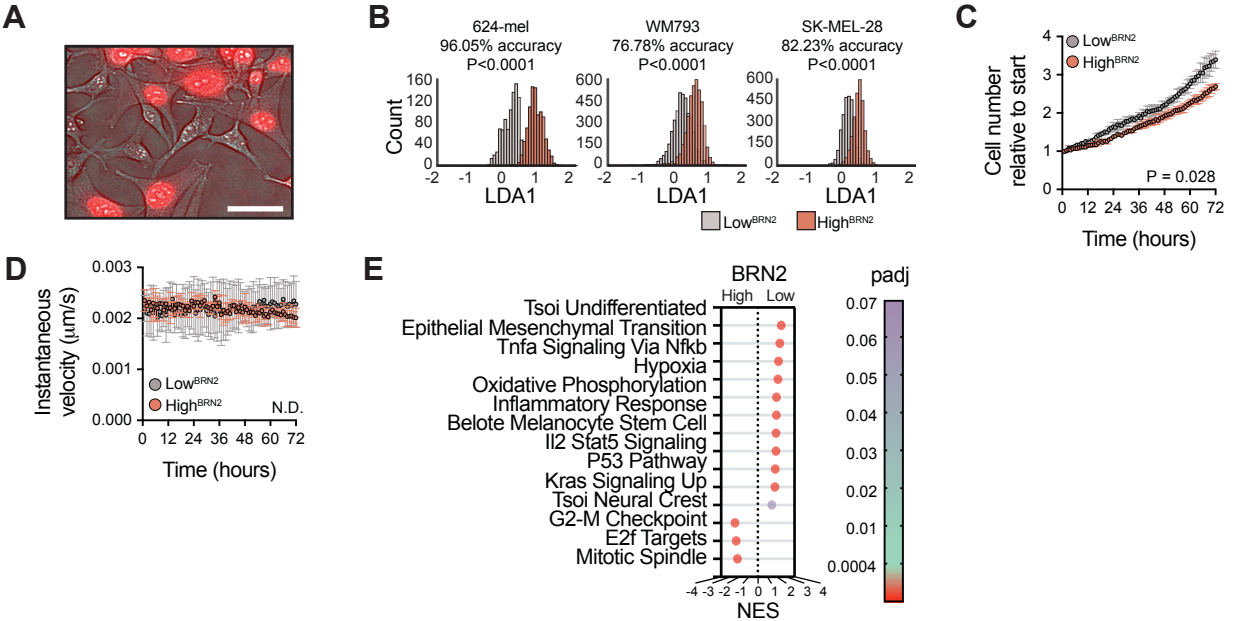
A
B
624-mel
96.05% accuracy
P<0.0001
WM793
76.78% accuracy
P<0.0001
SK-MEL-28
82.23% accuracy
P<0.0001
Count
LDA1
LowBRN2
HighBRN2
C
Cell number relative to start
P = 0.028
Time (hours)
D
Instantaneous velocity (μm/s)
N.D.
Time (hours)
E
BRN2
High
Low
padj
Tsoi Undifferentiated
Epithelial Mesenchymal Transition
Tnfa Signaling Via Nfkb
Hypoxia
Oxidative Phosphorylation
Inflammatory Response
Belote Melanocyte Stem Cell
Il2 Stat5 Signaling
P53 Pathway
Kras Signaling Up
Tsoi Neural Crest
G2-M Checkpoint
E2f Targets
Mitotic Spindle
NES

Figure 2

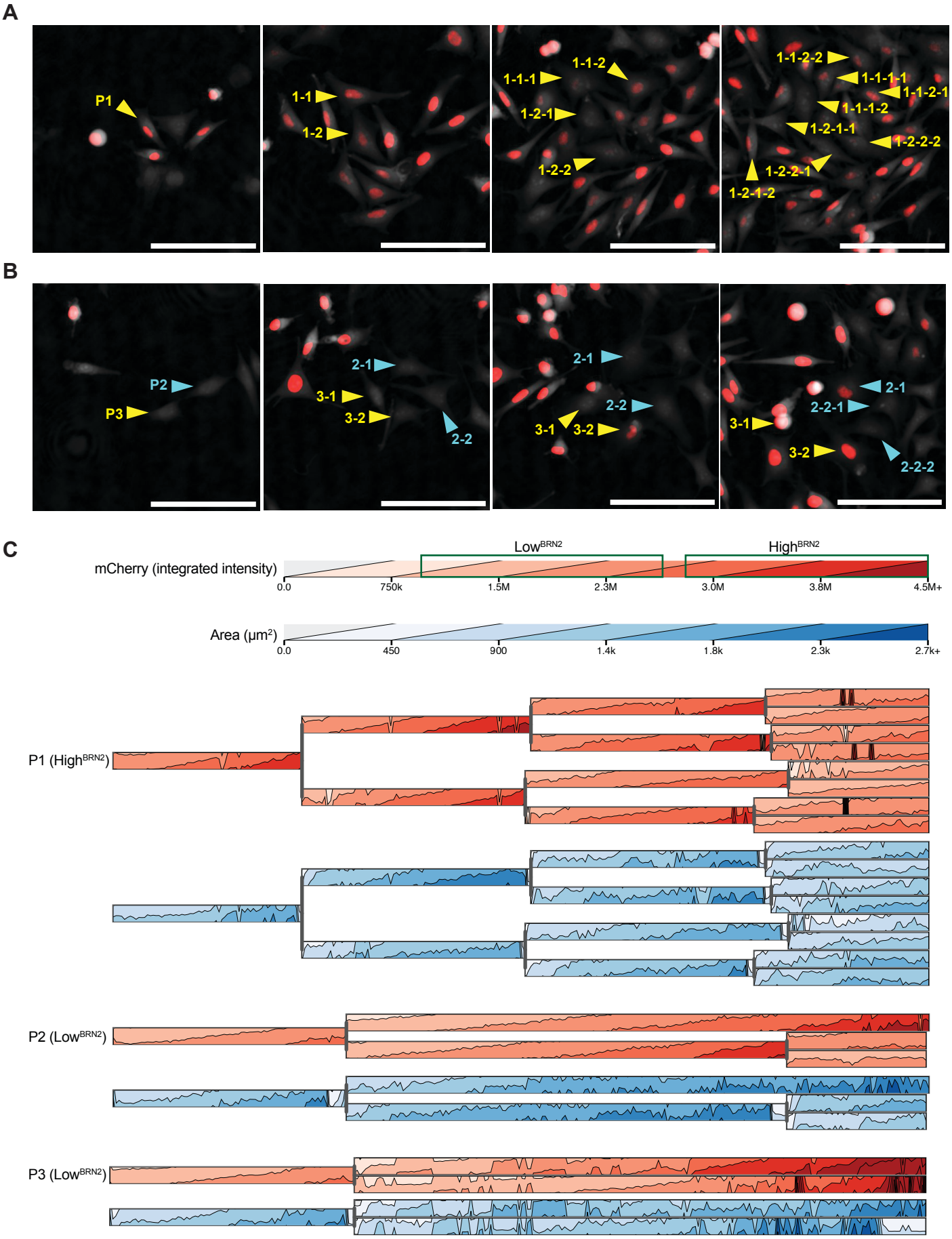
A
P1
1-1
1-2
1-1-1
1-1-2
1-2-1
1-2-2
1-1-2-2
1-1-1-1
1-1-2-1
1-1-1-2
1-2-1-1
1-2-2-2
1-2-2-1
1-2-1-2
B
P2
P3
2-1
3-1
3-2
2-2
2-1
2-2
3-1
3-2
2-1
2-2-1
3-1
3-2
2-2-2
C
mCherry (integrated intensity)
Low^BRN2
High^BRN2
0.0
750k
1.5M
2.3M
3.0M
3.8M
4.5M+
Area (μm²)
0.0
450
900
1.4k
1.8k
2.3k
2.7k+
P1 (High^BRN2)
P2 (Low^BRN2)
P3 (Low^BRN2)

Figure 3

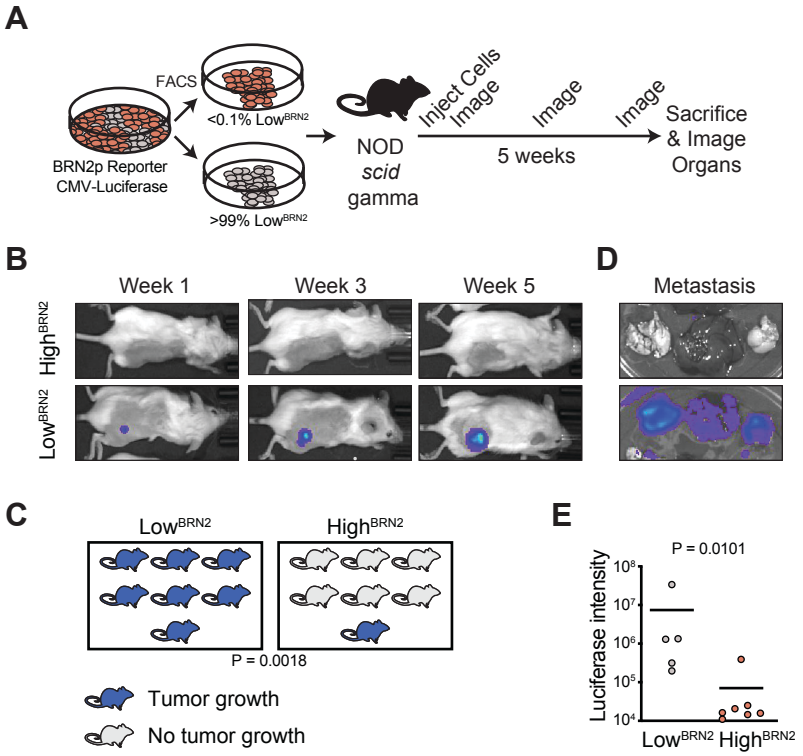
A
FACS
<0.1% Low^BRN2
>99% Low^BRN2
BRN2p Reporter
CMV-Luciferase
NOD
scid
gamma
Inject Cells
Image
Image
Image
5 weeks
Sacrifice
& Image
Organs
B
Week 1
Week 3
Week 5
High^BRN2
Low^BRN2
D
Metastasis
C
Low^BRN2
High^BRN2
P = 0.0018
Tumor growth
No tumor growth
E
P = 0.0101
Luciferase intensity
10^8
10^7
10^6
10^5
10^4
Low^BRN2
High^BRN2

Figure 4

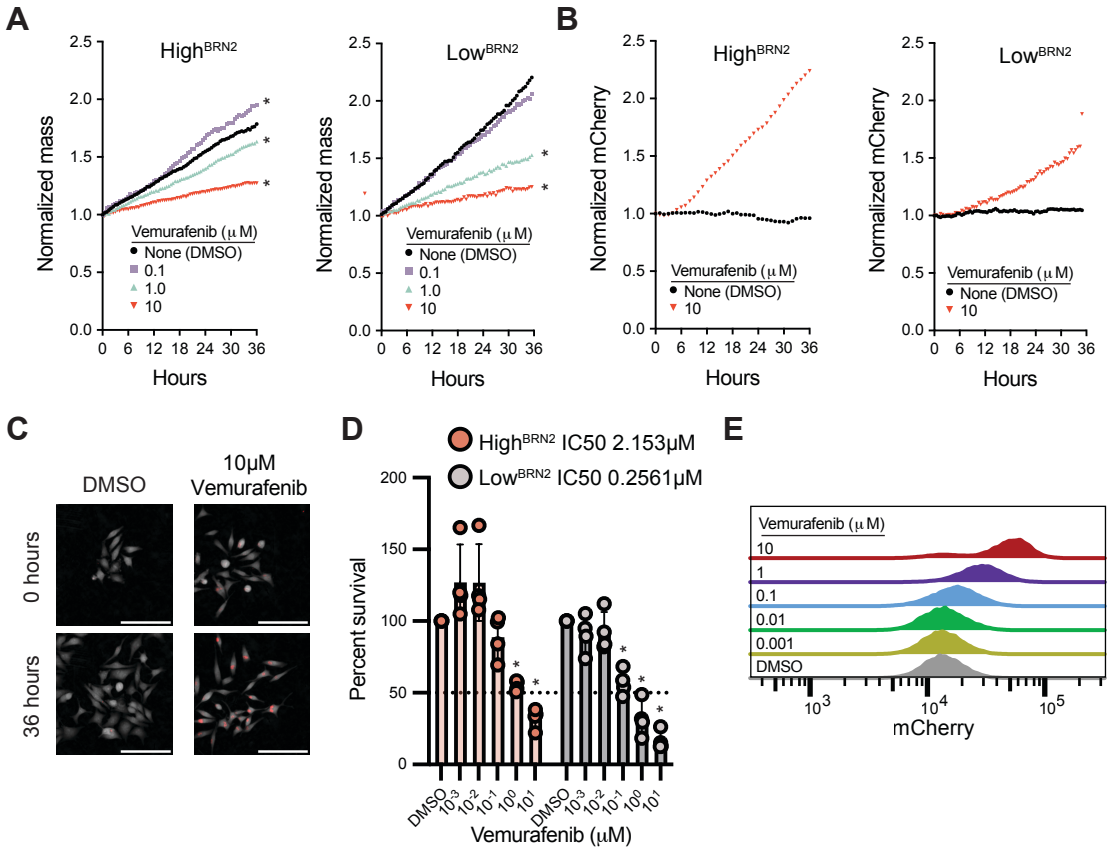
A
High^BRN2
Low^BRN2
Normalized mass
Hours
Vemurafenib (μM)
None (DMSO)
0.1
1.0
10
B
Normalized mCherry
C
DMSO
10μM Vemurafenib
0 hours
36 hours
D
High^BRN2 IC50 2.153μM
Low^BRN2 IC50 0.2561μM
Percent survival
Vemurafenib (μM)
E
Vemurafenib (μM)
10
1
0.1
0.01
0.001
DMSO
mCherry

Figure 5

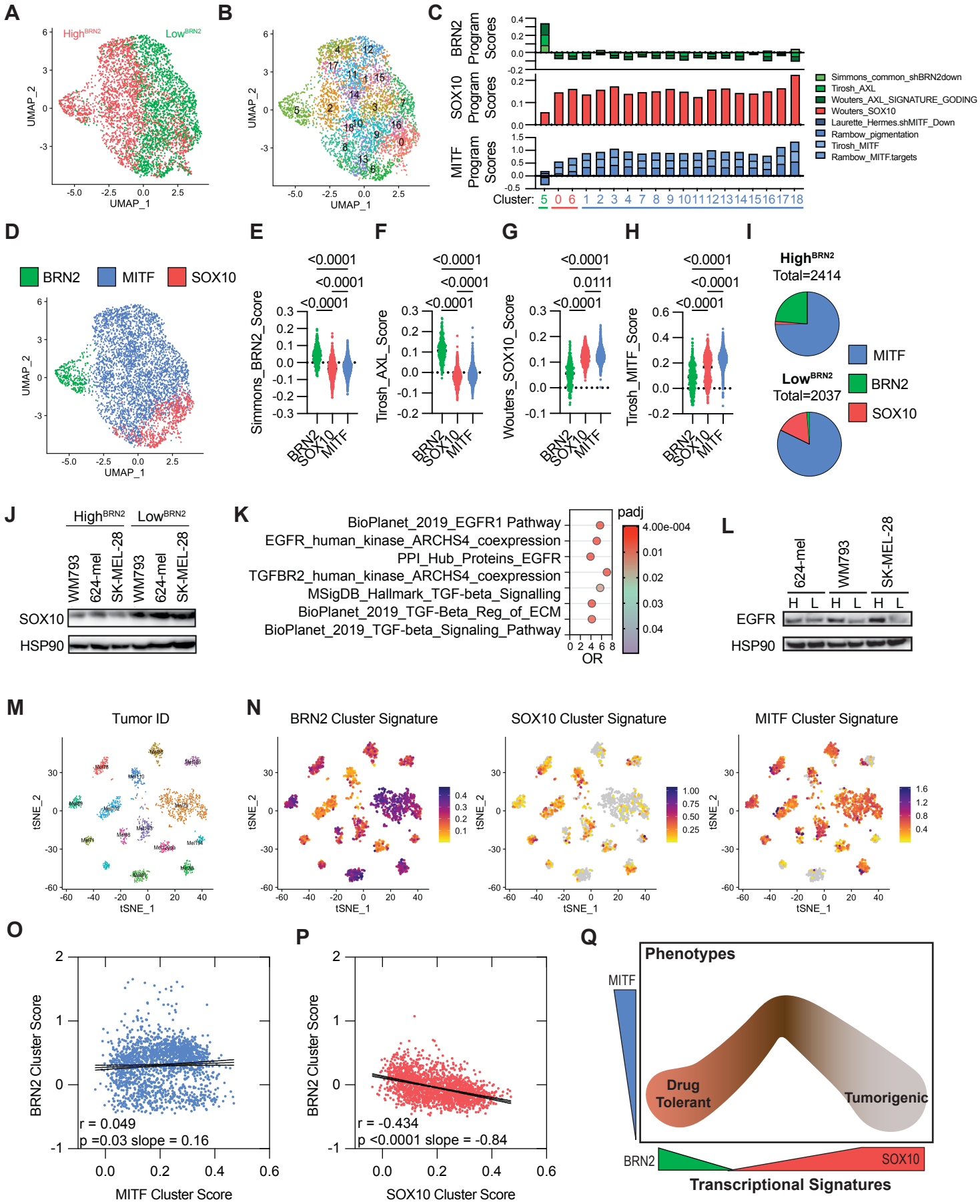
A
High BRN2
Low BRN2
UMAP_2
UMAP_1
B
C
BRN2 Program Scores
SOX10 Program Scores
MITF Program Scores
Cluster: 5 0 6 1 2 3 4 7 8 9 10 11 12 13 14 15 16 17 18
Simmons_common_shBRN2down
Tirosh_AXL
Wouters_AXL_SIGNATURE_GODING
Wouters_SOX10
Laurette_Hermes.shMITF_Down
Rambow_pigmentation
Tirosh_MITF
Rambow_MITF.targets
D
BRN2
MITF
SOX10
E
Simmons_BRN2_Score
F
Tirosh_AXL_Score
G
Wouters_SOX10_Score
H
Tirosh_MITF_Score
<0.0001
0.0111
I
High BRN2
Total=2414
Low BRN2
Total=2037
J
High BRN2
Low BRN2
WM793
624-mel
SK-MEL-28
SOX10
HSP90
K
BioPlanet_2019_EGFR1 Pathway
EGFR_human_kinase_ARCHS4_coexpression
PPI_Hub_Proteins_EGFR
TGFBR2_human_kinase_ARCHS4_coexpression
MSigDB_Hallmark_TGF-beta_Signalling
BioPlanet_2019_TGF-Beta_Reg_of_ECM
BioPlanet_2019_TGF-beta_Signaling_Pathway
padj
OR
L
624-mel
WM793
SK-MEL-28
H L H L H L
EGFR
HSP90
M
Tumor ID
tSNE_1
tSNE_2
N
BRN2 Cluster Signature
SOX10 Cluster Signature
MITF Cluster Signature
O
BRN2 Cluster Score
MITF Cluster Score
r = 0.049
p =0.03 slope = 0.16
P
SOX10 Cluster Score
r = -0.434
p <0.0001 slope = -0.84
Q
Phenotypes
MITF
Drug Tolerant
Tumorigenic
BRN2
SOX10
Transcriptional Signatures